Chemical Engineering Journal 521 (2025) 166480

Contents lists available at ScienceDirect

Chemical Engineering Journal

journal homepage: www.elsevier.com/locate/cej

Overcoming electron transfer bottleneck in CuS-biochar catalyst through interfacial Fe nanodots for enhanced peroxymonosulfate activation

Xinyi Zhang [a,b,c], Jian Wei [b,c,*], Zhuang Guo [b,c], Liangjie Wang [b,c], Junfeng Dou [a], Yonghui Song [a,b,c,*]

[a] College of Water Sciences, Beijing Normal University, Beijing 100875, China
[b] State Key Laboratory of Environmental Criteria and Risk Assessment, Chinese Research Academy of Environmental Sciences, Beijing 100012, China
[c] Institute of Water Ecology and Environment, Chinese Research Academy of Environmental Sciences, Beijing 100012, China

ARTICLE INFO

Keywords:
Bimetallic biochar catalyst
Interface engineering
Dual active center
Synergistic effect
Wastewater remediation

ABSTRACT

Developing high-efficiency catalysts for peroxymonosulfate (PMS) activation remains challenging due to sluggish electron transfer and unstable active sites in conventional monometallic-carbon systems. Herein, introducing interfacial metal iron nanodots into corn cores-based biochar (CCBC) loading copper sulfide composites (CuS@Fe-CCBC) achieved 27, 14, 4 and 3-fold improvement in the degradation on sulfamerazine (SMR) than CCBC, Fe-CCBC, CuS, CuS@CCBC with almost complete decomposition of PMS (99.2 %). Based on experiments and theoretical calculations, we confirmed that the CuS@Fe-CCBC catalyst promoted the adsorption and rapid electron transfer of PMS, which relied on the Fe-mediated electron bridge between CuS and CCBC. With S^{2-} species acting as electron donors during the dual redox cycling of Cu^{+}/Cu^{2+} and Fe^{2+}/Fe^{3+}, the O—O bonds and S—O bonds of PMS molecules were elongated and then broken. Afterwards, multiple reactive oxygen species (ROSs) were generated, including $^{\bullet}OH$, $SO_4^{\bullet-}$, $^1O_2$, and $O_2^{\bullet-}$ to contribute 28.1 %, 20.5 %, 46.7 % and 4.8 % on SMR removal. Besides, the degradation efficiency of SMR in the secondary effluent in the corresponding continuous-flow reactor was maintained more than 95 % for 180 h with allowable metal leaching (Cu < 0.5 mg/L, Fe < 0.15 mg/L). This study provides important insights into the practical application of PMS activation process and offers a sustainable solution for the deep purification of wastewater.

1. Introduction

Over the past decades, widely used broad-spectrum antibiotics are not fully metabolized by organisms, then enter wastewater treatment plants (WWTP) or directly into the aquatic environment in raw or metabolic intermediate state [1]. The global water crisis has been exacerbated by the recalcitrance of these residual antibiotic to mainstream biological treatment technologies [2]. The persistence of antibiotic residues in the environment propagates antibiotic resistance genes [3]. Antimicrobial resistance has already been recognized by the World Health Organization as a major global health threat [4]. Globally, multidrug-resistant pathogens cause approximately 700,000 deaths annually [5]. Due to their ecological risks and adverse human health effects, antibiotics are prominent emerging contaminants. Based on risk entropy assessment and prioritization for treatment, sulfonamides were found to contain the highest number of antibiotics requiring focused attention out of 129 antibiotics detectable in the aquatic environment [6]. Sulfamerazine (SMR), as a representative sulfonamide, is widely used to treat infectious diseases. Most SMR released from hospitals, pharmaceutical factories, and livestock farms into WWTP or water bodies which can be detected at concentrations of ng/L to mg/L [7]. However, even at trace levels, SMR remains ecotoxic to aquatic organisms while triggering pathogenic microorganisms, bacteria to develop antibiotic resistance genes (ARGs), jeopardizing ecosystems and human health [8]. Hence, the rising demand for effective removal of trace level and cumulative antibiotics has led to a boom in the development of advanced oxidation processes (AOPs).

Among prevailing AOPs, peroxymonosulfate-based AOPs (PMS-AOPs), with inexpensive core oxidant, more stable and safer in storage and transportation, diverse reactive oxygen species (ROSs) under flexible regulation for targeted generation, is superior than traditional AOPs [9–11]. Relying on oxidizing ability of PMS itself, refractory organic

* Corresponding authors at: State Key Laboratory of Environmental Criteria and Risk Assessment, Chinese Research Academy of Environmental Sciences, Beijing 100012, China.
E-mail addresses: weijian0911@163.com (J. Wei), songyh@craes.org.cn (Y. Song).

https://doi.org/10.1016/j.cej.2025.166480
Received 30 April 2025; Received in revised form 14 July 2025; Accepted 25 July 2025
Available online 29 July 2025
1385-8947/

pollutants degradation is limited. It commonly needs to be activated by heat, light, ultrasound, alkali, homogeneous or heterogeneous activators [12]. Obviously, simple and effective activation is particularly notable by multivalent redox cycling reactions of transition metals (*e.g.*, Fe, Co, Cu, Mn), which provide electron acceptors and electron donors for asymmetric PMS (H—O—O—SO_3^-) molecules [13]. As mentioned earlier, the production of multiple ROSs was involved in PMS-AOPs. The studies on their identification, quantification, and contribution calculation must be comprehensive and rigorous. A relatively well-established set of protocols has been reported in the midst of continuing controversy over the study methodology [14]. However, the identification of ROSs remained be neglected and unsystematic in most studies. The electron transfer process that occurs during bond breaking of PMS molecules was also unclear to some degree.

Copper-based catalysts have received much attention in the last decade due to their effective activity in PMS activation with the most diverse activation pathways [15,16]. Among them, copper-based sulfides are considered as promising catalysts as the main electron donors for the PMS activation process [17,18]. This mainly due to the cascading oxidation process of sulfur species (S^{2-}) powers the regeneration of metal sites to enhance the sustained activation of PMS [19]. Especially, the unique ultra-simple fabrication process of CuS (rapid grinding) stands out from many other catalysts that require high temperature and pressure, multiple synthesis aids [20]. However, this method has not yet been applied in the CuS loading process of composite materials. Besides, the application of CuS is still hindered by their aggregation, passivation and metal leaching. Biochar (BC), as an advantageous carbon substrate, stands out with rich surface functional groups, low cost, and porous structure [10], which can provide more reactive sites, introduce more ROSs, and inhibit metal ion leaching [21,22]. Corn has been an important consumer product worldwide. According to the report from United States Department of Agriculture (USDA), the global production of corn in 2024 could reach 1.213 billion tons. A large amount of corn cores are generated as bio-waste, which is considered a sizable raw material for BC production [23].

In the single CuS-loaded BC system, the semiconductor property of CuS (band gap of about 1.5–2.2 eV) leads to low intrinsic conductivity [18]. The heterogeneous interface between CuS and BC is prone to the formation of Schottky barriers, which hinders the electron migration from BC to CuS [24]. Introducing a functional Fe intercalation to form a CuS-Fe-C interface can reduce the interfacial resistance because functional Fe forms a continuous conductive pathway with the sp^2 carbon structure of the BC, which can enhance the overall charge separation and transfer [10,19,25]. In addition, the establishment of the Cu—Fe bimetallic activation center could set up a self-sustained oxidation chain [26], based on the fact that the redox potential of Fe ($E_0(Fe^{3+}/Fe^{2+})$ = 0.77 eV) is greater than that of Cu ($E_0(Cu^{2+}/Cu^{+})$ = 0.34 eV), which can initiate the reaction of $Fe^{3+} + Cu^{+} \rightarrow Fe^{2+} + Cu^{2+}$ [27,28]. In this process, Cu^{+} would play the dual roles of activating PMS and promoting the regeneration of Fe^{2+}, simultaneously. Meanwhile, the more dispersed Cu^{2+} due to the strong oxidation of Fe^{3+} was also conducive to the regeneration of Cu^{+} afterwards, which effectively solving the problem of passivation of metal active sites.

In summary, previous studies on bimetallic materials have focused on the activation of PMS using synergistic redox cycles of bimetals for efficient degradation of pollutants. Alternatively, the development of carbon-based materials has mainly taken advantage of their high porosity, abundant functional groups (—COOH, —OH), and tunable surface chemistry to assist metal catalysts in activating PMS. However, less attention has been paid to the electron transfer resistance that exists between carbon-based materials and metal components. The idea of utilizing interlayer metal nanodots to facilitate the electron transfer between the carbon substrate and the metal active component has rarely been investigated. In addition, the shortcomings of the current studies on PMS-AOPs were taken into account. Our work achieved a maximum refinement of ROSs identification, as well as a detailed investigation of the electron transfer process during PMS decomposition.

In this study, CuS was loaded on iron-doped corn cores biochar (CuS@Fe-CCBC) firstly using a simple rapid grinding method, aiming at constructing an active medium (Fe) between CuS and BC substrate to activate PMS for long-term and effective degradation of typical antibiotics. Our work focuses on 1) characterizing the physicochemical properties of the prepared CuS@Fe-CCBC composite; 2) evaluating its catalytic performance for activating PMS using SMR as the target pollutant; 3) identifying the major reactive oxygen species (ROSs) in the reaction system and calculating their contributions; 4) elucidating the intrinsic mechanism of the synergistic activation of the PMS by CuS and the metal Fe; 5) verifying the long-term operational stability of a continuous flow reaction column based on CuS@Fe-CCBC/PMS in complex water bodies. This work demonstrated the potential application of the CuS@Fe-CCBC/PMS system for the deep mineralization of antibiotics in wastewater and offered a critical reference for the practical application of PMS-AOPs.

2. Materials and experiments

2.1. Materials and reagents

Corn cores were collected from agricultural wastes in northeastern China. Peroxymonosulfate (PMS, $KHSO_5{\cdot}0.5KHSO_4{\cdot}0.5K_2SO_4$, ≥42 % $KHSO_5$ basis), sodium thiosulfate pentahydrate ($Na_2S_2O_3{\cdot}5H_2O$), sulfamerazine (SMR), atrazine (ATZ), pemetrynone (PMD), diclofenac sodium (DCF), sulfadimethoxine (SAT) and carbamazepine (CBZ) were purchased from Aladdin Reagent Co., Ltd. (Shanghai, China). Ferrous chloride ($FeCl_2{\cdot}4H_2O$), copper nitrate ($Cu(NO_3)_2{\cdot}3H_2O$), sodium sulfide ($Na_2S{\cdot}9H_2O$), tertiary butanol (TBA), methyl alcohol (MeOH), furfuryl Alcohol (FFA), p-benzoquinone (p-BQ), 5,5-Dimethyl-1-Pyrrolidinium N-oxide (DMPO), 2,2,6,6-tetramethyl-4-piperidinol (TEMP), p-Hydroxybenzoic acid (p-HBA), 1,3-diphenylisobenzofuran (DPBF), nitrotetrazolium blue chloride (NBT), formazan were provided by Sinopharm Chemical Reagent Co., Ltd. (Beijing, China). Other reagents were offered in the Text S1. All chemicals used in this study were analytical standard grade products with >99 % purity, unless otherwise stated, and the deionized water (18 MΩ·cm) was used for most experiments.

2.2. Catalysts fabrication

Corn cores were sieved through a 10-mesh sieve and rinsed three times each with deionized water and ethanol, dried at 60 °C then. Subsequently, 1.5 g of corn cores was immersed in $FeCl_2{\cdot}4H_2O$ solution (8 mM) and stirred at room temperature for 12 h. After drying at 80 °C, it was loaded into a tube furnaces and heated up at a rate of 5 °C/min under N_2 atmosphere, and finally the pyrolysis temperature was maintained at 800 °C for 2 h. The obtained Fe-CCBC above with different calcination temperatures were prepared according to the same method. CCBC was prepared by direct calcination without impregnation with $FeCl_2{\cdot}4H_2O$ solution for reference.

0.251x g of $Cu(NO_3)_3{\cdot}3H_2O$, 0.249x g of $Na_2S{\cdot}9H_2O$ and 0.1y g of Fe-CCBC were placed in a mortar. After sufficiently grinding for 5 min, product was washed with deionized water and ethanol for several times. Subsequently, it was dried at 90 °C for 6 h to obtain CuS@Fe-CCBC (x:y) composites. Herein, the values of x, y above referred to the pre-set mass ratio of CuS:Fe-CCBC in composite, which were taken integer. By weighing a fixed multiple of raw materials mentioned before in the ratio of x:y, CuS@Fe-CCBC (x:y) composites with relatively precise mass ratios could be synthesized. The single CuS preparation and synthesis of CuS@CCBC were also carried out following this rapid grinding method. Multiple batches of CuS@Fe-CCBC samples synthesized in this study *via* the rapid grinding method maintained a high degree of consistency in terms of loading efficiency, particle dispersion uniformity and degradation properties with excellent reproducibility. In addition, Na_2S as one of the core raw materials in this study proved to be the best choice of

sulfur source [20].

2.3. Experimental procedure

Batch experiments were conducted in a thermostatic water bath at 25 °C with a mechanical stirring paddle speed of 350 r/min. Catalyst and PMS were injected into the simulated pollutant solution at an initial concentration of 5 mg/L to initiate the reaction. At fixed time intervals, reaction samples were drawn through a 0.22 μm polyethersulfone filter, while $Na_2S_2O_3$ solution was added to terminate the reaction, waiting for further detection. In order to investigate the reuse effect of the material, the catalyst after the reaction was collected, washed and dried several times for the next degradation experiment. For avoiding the extra loss, several sets of experiments were set up in parallel at the same time.

2.4. Characterization and analysis

A series of characterizations of the physicochemical properties of various catalysts were carried out. The involved methods were supplied in Text S2. In addition, including contaminant concentration detections and intermediate product assays, electrochemical measurements, *in-situ* test procedures *etc.* were described in Table S1 and Text S3.

2.5. DFT calculation

The methods in the density functional theory (DFT) calculations of this study were provided in Text S4. Herein, we simplified DFT calculations model of biochar as a substrate composed of C atoms [29]. It is important to note the limitations of this simplified approach; real biochar has a more complex composition and its porous structure is usually rich in defects, heteroatoms and oxygen-containing functional groups. Therefore, when the reaction mechanism involves above specific structures in BC, the model of which cannot be simplified using a graphene structure.

3. Results and discussion

3.1. Characterization of catalysts

The *in-situ* loading of CuS was achieved by rapid milling of Cu $(NO_3)_2{\cdot}3H_2O$ and $Na_2S{\cdot}9H_2O$ on Fe-impregnated calcined corn cores biochar to obtain CuS@Fe-CCBC, the specific process was illustrated in Fig. 1a. Prior to the study of the composites, the calcination temperature of the Fe-CCBC was systematically optimized and screened, while the Fe-CCBC calcined at 800 °C was finally identified as the dominant carrier. Details were described in Text S5, Figs. S1–S2 and Table S2. As revealed in Fig. 1b–e, scanning electron microscopy (SEM) images elucidated distinct morphological and compositional distribution of several samples. CCBC presented a honeycomb-like structure consisting of thin carbon layers (Fig. 1b). Fe particulates were successfully achieved uniform dispersing on the CCBC layers (Fig. 1c), while CuS nanoparticle agglomeration (Fig. 1d) could be observed on the final CuS@Fe-CCBC composites as well (Fig. 1e). The corresponding elemental mapping (Fig. 1f) revealed homogeneous spatial distribution of C, O, Fe, Cu, and S. With high-resolution transmission electron microscopy (HR-TEM) observation (Fig. S3a–b), the lattice spacings of 0.19 and 0.28 nm were consistent in the (110) and (102) planes of CuS [13,30], while the Fe species (0.86 nm spacing) encapsulated within CCBC graphitic carbon layer (0.34 nm spacing) [31]. The interface where CuS, Fe particles, and the CCBC substrate met was also identified and labeled in Fig. S3b.

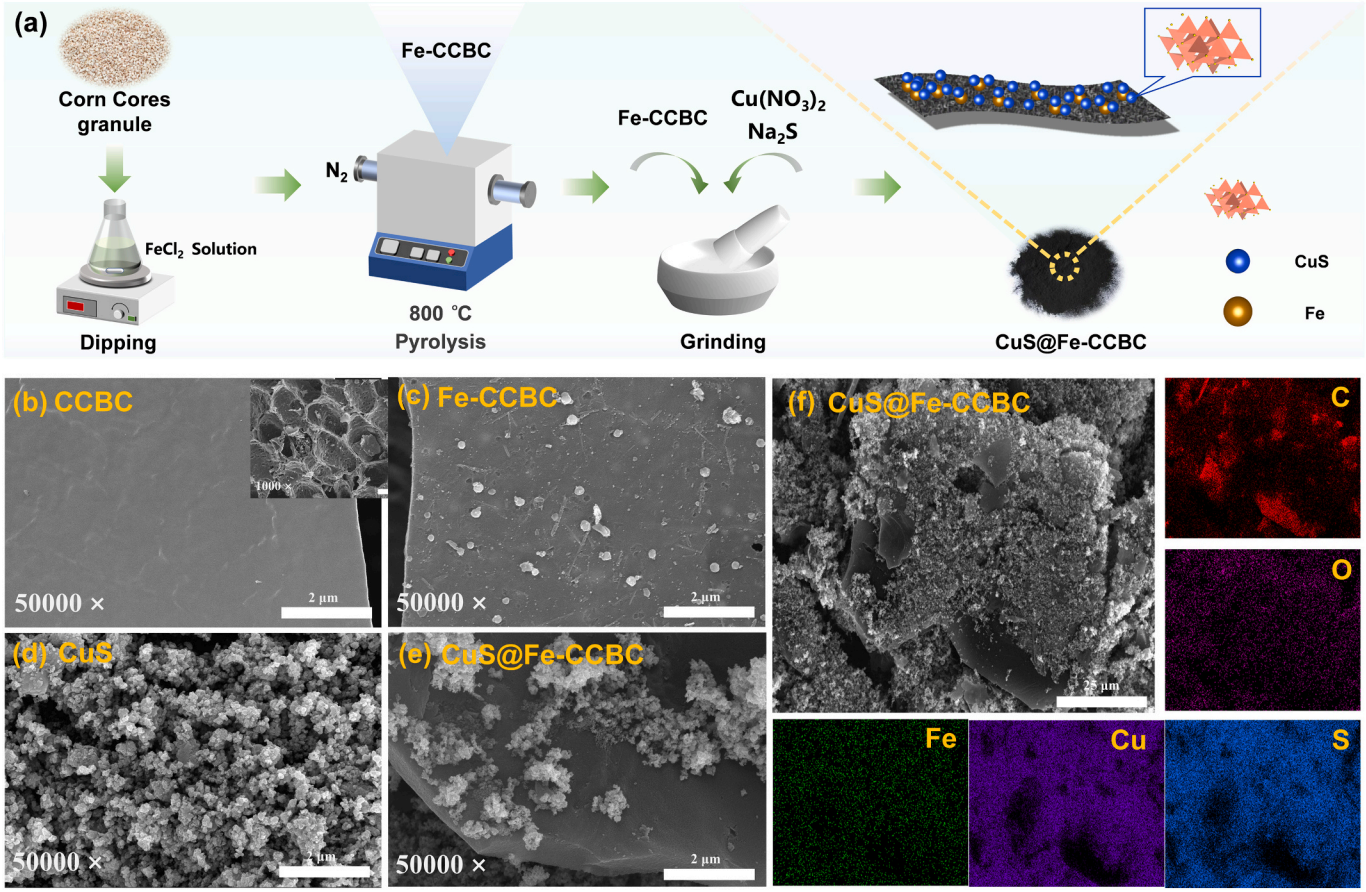

Fig. 1. (a) Schematic illustration of CuS@Fe-CCBC synthesis procedures. SEM images of (b) CCBC, (c) Fe-CCBC, (d) CuS and (e) CuS@Fe-CCBC. (f) Energy dispersive spectroscopy mapping images of C, O, Fe, Cu and S in CuS@Fe-CCBC.

The crystal structures of all the materials were analyzed by XRD patterns (Fig. 2a). CCBC exhibited amorphous and crystalline carbon peaks belonged to (002) and (100) facets, respectively [32]. Fe-CCBC possessed functional iron diffraction peaks at 44.7° (110), 65.0° (200) and 82.3° (211) (JCPDS#06-0696) with a residual amorphous carbon [33]. Meanwhile, Fe nanodots were assigned with Fe_3O_4 (220) at 30.1°, Fe_3O_4 (311) at 35.4°, Fe_3C (102) at 43.7° and Fe_3C (122) at 51.8°, according to JCPDS#19-0629 and JCPDS#35-0772. The XRD patterns of CuS were consistent with the standard card of covellite (JCPDS#06-0464) [24]. All these characteristic peaks could be observed in CuS@Fe-CCBC. The blue dashed lines represented the characteristic peaks belonging to CuS, while the green crystal surface labeling represented the characteristic peaks belonging to Fe species on CCBC. It could be indicated that CuS was successfully synthesized on the Fe-CCBC, which was in accordance with the TEM results. The disappearance of characteristic peaks for CCBC might be caused by too much metal cover [29,34,35]. Including CCBC, Fe-CCBC, CuS and CuS@Fe-CCBC, the apparent absorption peak near 3400 cm^{-1} in the Fourier transform infrared (FTIR) spectroscopy (Fig. 2b) were attributed to —OH stretching vibrations [36]. The characteristic peaks at 1588 cm^{-1}, 1099 cm^{-1} and 1004 cm^{-1} coincided with C═C, C—O and C═O bonds [37–39].

Raman spectra (Fig. 2c) displayed the signals at ~1340 cm^{-1} and ~1590 cm^{-1} for defects of carbon atomic crystal (I_D) and graphite phase (I_G) in CCBC based materials. CCBC, Fe-CCBC and CuS@Fe-CCBC owned the similar I_D/I_G ratio as 0.97, 0.98 and 0.99, implying that the introduction of Fe nanodots and CuS would not cause more defective sites formation in the composites, which might contribute little to the activation of PMS [40]. In addition, the N_2 adsorption-desorption curves (Fig. 2d–e, Table S3) revealed all catalysts possessed typical type IV isotherms with H4 hysteresis loops, confirming their mesoporous structure with irregular pore geometries [41]. Moreover, X-ray photoelectron spectroscopy (XPS) illustrated the existed element on the as-prepared materials. The inclusion of C 1s, O 1s, Fe 2p, Cu 2p and S 2p was confirmed by XPS survey of CuS@Fe-CCBC in Fig. 2f. From Fig. S4a–d, the fitted XPS spectra for CCBC, Fe-CCBC, CuS and CuS@Fe-CCBC was investigated in detail. The C—C, C—O—C, C═O and π-π* bonds were found both in CCBC, Fe-CCBC and CuS@Fe-CCBC. As for element O 1s, beside C—O and C═O groups in CCBC, Fe-CCBC and CuS@Fe-CCBC, metal-O bond was increased in Fe-CCBC and CuS@Fe-CCBC. Functional Fe nanodots in Fe-CCBC existed as Fe^{2+} (48.18 %) and Fe^{3+} (51.82 %), while the contents of which were 66.95 % (Fe^{2+}) and 33.05 % (Fe^{3+}) in CuS@Fe-CCBC. Compared with isolated CuS, the ratio of Cu^{+} decreased from 56.26 % to 38.72 %, while the ratio of Cu^{2+} increased from 43.74 % to 61.28 %. Moreover, the content of oxidized S species (S_2^{2-}, S_n^{2-} and SO_4^{2-}) in the composites increased accordingly. These were all attributed to the reduction of Fe species in CCBC provided by the introduction of CuS [42]. All in all, these results substantiated that CuS@Fe-CCBC composite was successfully fabricated.

3.2. Performance evaluation of catalysts

Sulfamerazine (SMR) was selected as a target contaminant to evaluate the PMS activation performance in different systems. Initially, Fig. S5a–b revealed the effects of different CuS/Fe-CCBC composite ratios on SMR degradation efficiency. The adsorption process was negligible in the first 30 min. As the proportion of CuS increased to 3:1, the degradation efficiency of SMR was gradually improved to 96.1 % within 40-min reaction (k_{obs} = 0.082 min^{-1}). However, the removal effect was limited when the CuS ratio exceeded 3:1, which was then determined as a dominant one for the entire research.

As shown in Fig. 3a, all the catalysts possessed poor adsorption ability for SMR in the absence of PMS with previous 30 min. Notably, PMS alone exhibited negligible degradation efficiency toward SMR (<12 % over subsequent 40 min). With the further addition of PMS, CuS@Fe-CCBC displayed the greatest degradation performance (96.1 %), surpassing the efficiencies observed in the system of CCBC/PMS (13.2 %), Fe-CCBC/PMS (22.9 %), CuS/PMS (56.6 %) and CuS@CCBC/PMS (73.9 %). As depicted in Fig. 3b, the reaction kinetic constants (k_{obs}) of CuS@Fe-CCBC for PMS activation reached 0.082 min^{-1}, which were 27-, 14-, 4- and 3-fold higher than those of CCBC, Fe-CCBC, CuS and CuS@CCBC, respectively. Moreover, the synergy index of CuS and Fe calculated by $\eta = k_{CuS@Fe\text{-}CCBC/PMS}/(k_{Fe\text{-}CCBC/PMS} + k_{CuS@CCBC/PMS})$ was 2.1, while the PMS consumption efficiency of which (99.2 %) had remarkable advantage compared with Fe-CCBC/PMS (17.3 %) and CuS@CCBC/PMS (79.9 %) from Fig. 3c, confirming synergistic effect in CuS@Fe-CCBC enhanced PMS decomposition activity. Notably,

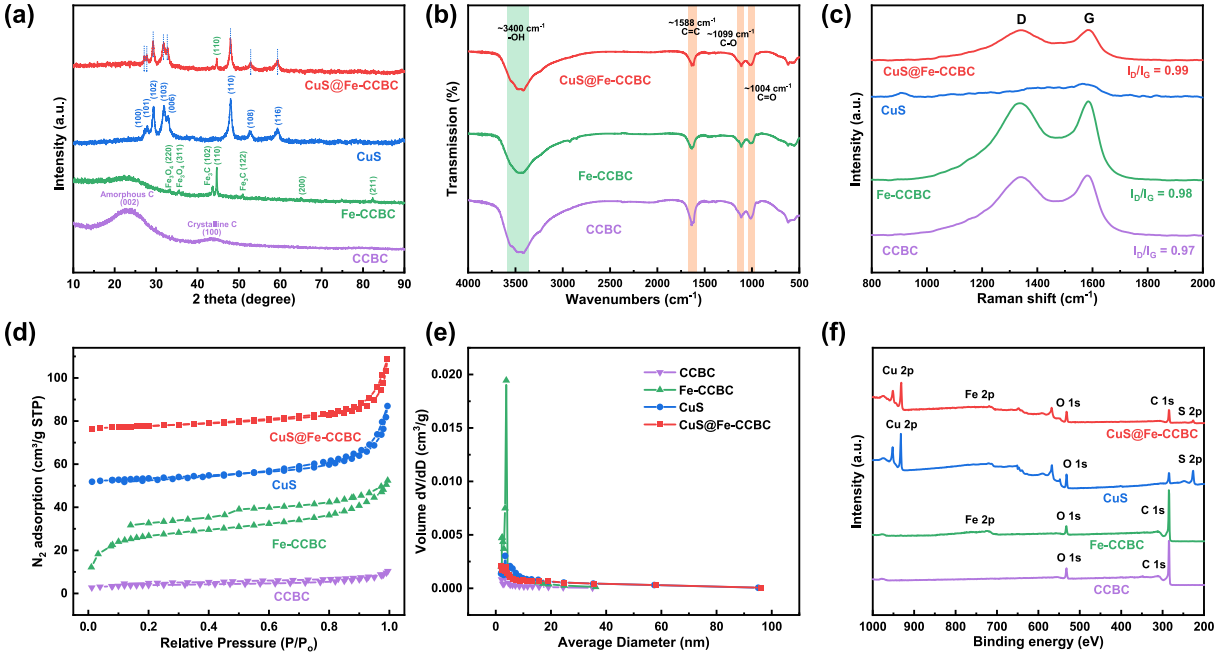

Fig. 2. (a) XRD patterns, (b) FTIR spectras, (c) Raman spectras, (d) N_2 adsorption-desorption isotherms curves, (e) pore size distribution curves and (f) XPS survey spectras of various samples.

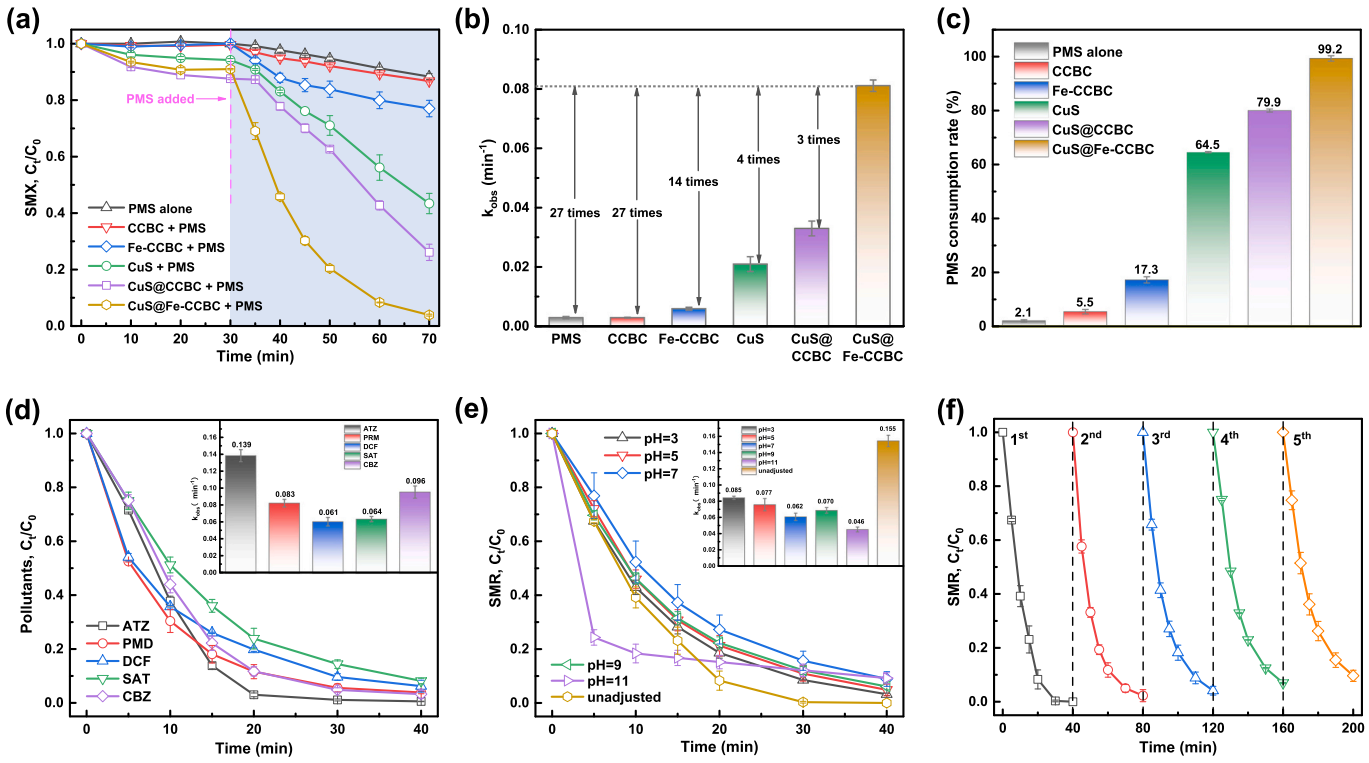

Fig. 3. (a) The SMR degradation efficiency, (b) corresponding reaction rates and (c) PMS consumption rates in different systems. (d) Different pollutants removal rates with the treatment of CuS@Fe-CCBC/PMS. (e) The effect of initial pH on degradation efficiency in CuS@Fe-CCBC/PMS system. (f) The reusability of CuS@Fe-CCBC in 5 runs. Fixed experiments conditions: $[SMR]_0$ = 5 mg/L, $[PMS]_0$ = 0.3 mM, $[Catalyst]_0$ = 100 mg/L, T = 25 °C, and initial pH = 5.57.

compared with CuS alone, the better performance of CuS@CCBC on PMS activation was attributed to the high porosity, abundant functional groups (—COOH, —OH), and tunable surface chemistry of biochar supporting. It enabled superior metal dispersion, strong anchoring, and enhanced electron transfer, boosting catalytic activity and stability. Regarding the CuS@Fe-CCBC/PMS system, the effects of PMS, catalyst dosage and SMR concentration on its characteristics were investigated in Fig. S6 and Text S6, while the total organic carbon (TOC) of which could be mineralized by 41.3 % (Fig. S7). By comparing the effect of CuS@Fe-CCBC with that of the more studied monometallic or bimetallic catalysts for the activation of PMS on the degradation of SMR, it was found that the optimal degradation effect was achieved by CuS@Fe-CCBC within 40-min reaction at a fixed catalyst and oxidant dosage (Fig. S8). Furthermore, the active performance of CuS@Fe-CCBC/PMS was more excellent than that of most of the previously reported other typical bimetallic and carbon-based catalysts/PMS systems for degrading pollutants (Fig. S9, Table S4).

Furthermore, the CuS@Fe-CCBC/PMS system exhibited superior degradation performance for recalcitrant organic pollutants, including atrazine (ATZ), primidone (PMD), diclofenac sodium (DCF), sulfadimethoxine (SAT), and carbamazepine (CBZ). The selection of specific pollutants were mainly attributed to the fact that: 1) They were difficult to eradicate by existing technologies in conventional wastewater treatment plants; 2) They were difficult to be decomposed naturally and persisted in the water environment, causing frequent detection; 3) They were difficult to be degraded by oxidizers (PMS, O_3 or H_2O_2) directly and required the assistance of activators [43–47]. Over 90 % degradation efficiency with a reaction rate exceeding 0.06 min^{-1} was achieved within 40 min (Fig. 3d). Meanwhile, CuS@Fe-CCBC/PMS system realized more than 90 % of SMR removal within pH set as 3–11 (Fig. 3e), demonstrating its broad pH adaptability. The pH monitoring revealed reactions consistently stabilized below pH = 7.5 across above range (Fig. S10a). Zeta potential analysis of CuS@Fe-CCBC identified the point of zero charge at pH = 7.43 (Fig. S10b), suggesting the enhanced contact between the electron-rich PMS and catalyst below this threshold governed the pH resilience of system.

The system of CuS@Fe-CCBC/PMS maintained stable degradation performance (Fig. 3f) with only slight decrease of 9.6 % in the fifth cycle. The apparent rate constants (Fig. S11a) showed a certain degree of decline during the five runs, which might be ascribed to the loss of some active sites on the catalyst surface during the oxidation process. It was remarkable that the dissolved concentration of metal ions after 5 recycle were 0.49 mg/L for Cu and 0.17 mg/L for Fe (Fig. S11b), which were all below the standard limit value of 0.5 mg/L (Cu) and 0.3 mg/L (Fe) in China (GB 18918-2002) and (GB 3838-2002).

3.3. Identification and contribution of ROSs

To investigate the reactive oxygen species (ROSs) produced in the CuS@Fe-CCBC/PMS system, quenching experiments (Fig. 4a) were implemented for the ROSs (•OH, $SO_4^{\bullet-}$, $^1O_2$, and $O_2^{\bullet-}$) that might be produced during the activation of PMS. With the detail analyses in Text S7, the shielding of above ROSs adversely affected the degradation of the system. To further clarify the active substances presented in the CuS@Fe-CCBC/PMS system, the electron paramagnetic resonance (EPR) detection was conducted. The intensities of DMPO-•OH and DMPO-$SO_4^{\bullet-}$ adduct signals increased temporally in Fig. 4b, while no detectable adduct formation without activator. Concurrent detection of classic peaks for DMPO-$O_2^{\bullet-}$ confirmed its presence during the catalytic reaction progressing (Fig. 4c). The characteristic TEMP-$^1O_2$ triplet signals were observed significantly greater magnitude than PMS controls, suggesting $^1O_2$ generation through PMS decomposition (Fig. 4d). Thus, the CuS@Fe-CCBC/PMS system consists of the existence of multiple ROSs referred above.

During PMS activation, $O_2^{\bullet-}$ are generated by electron capture from dissolved oxygen or by the reaction of PMS (HSO_5^-) with H_2O molecules [48]. According to the results of Fig. S12, the degradation efficiency of SMR was not inhibited in N_2 atmosphere and was not promoted in O_2

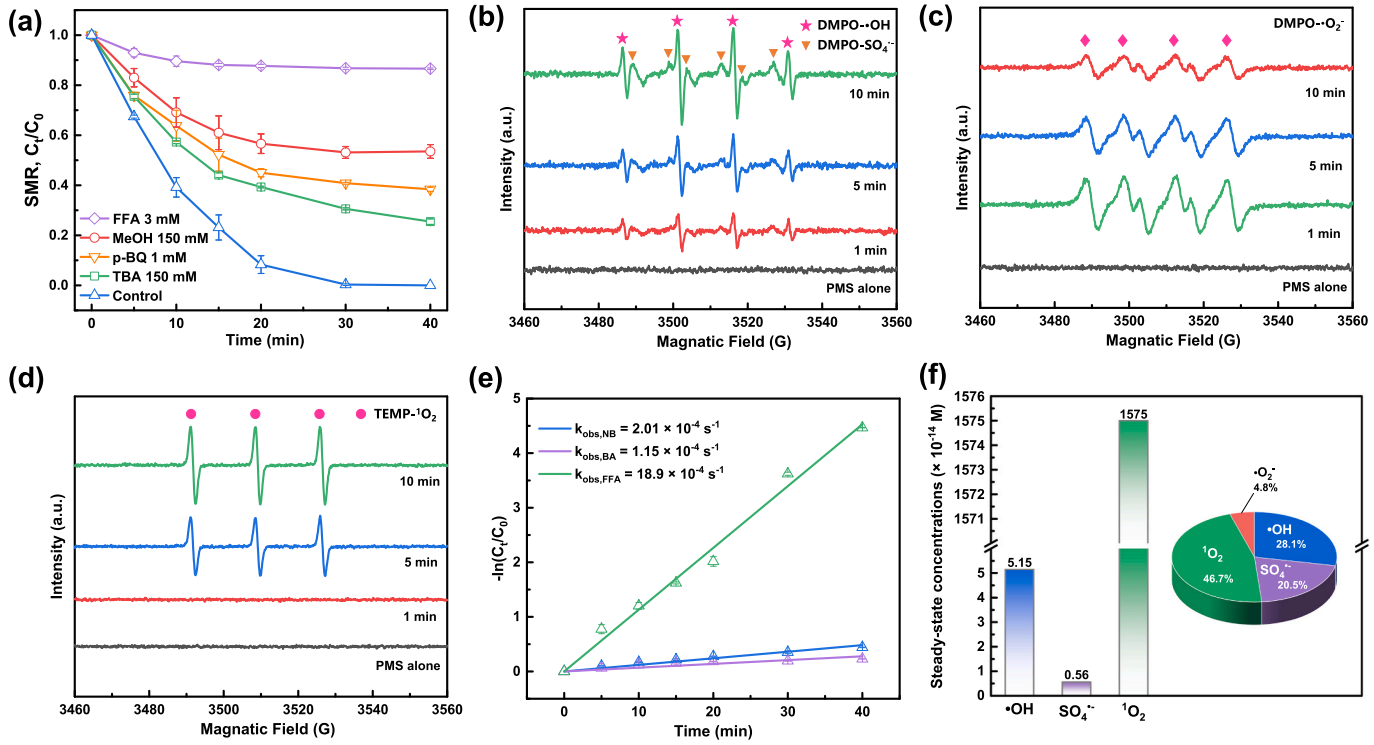

Fig. 4. (a) Quenching experiment for the CuS@Fe-CCBC/PMS system. EPR signal for (b) •OH, $SO_4^{•-}$ and (c) $O_2^{•-}$ captured by DMPO, (d) $^1O_2$ captured by TEMP in CuS@Fe-CCBC/PMS systems with PMS alone as reference. (e) The reaction kinetics of NB, BA and FFA (in MeOH) by CuS@Fe-CCBC/PMS system. (f) The relative steady-state concentration of •OH, $SO_4^{•-}$, $^1O_2$, and ROSs' contribution. Experiments conditions: $[SMR]_0$ = 5 mg/L, $[PMS]_0$ = 0.3 mM, $[Catalyst]_0$ = 100 mg/L, T = 25 °C, and initial pH = 5.57.

atmosphere, indicating that the reaction between HSO_5^- and H_2O mainly occurred to generate $O_2^{•-}$. Notably, the EPR signals of DMPO-$O_2^{•-}$ gradually weakened with the reaction processing (Fig. 4c), implying that the proton-promoted disproportionation of $O_2^{•-}$ in this system might be a way for $^1O_2$ formation [12,48]. Using 4-chloro-7-nitrobenzofurazan (NBD-Cl) as a probe compound, the fluorescence method was conducted to determine the concentration of $O_2^{•-}$. It was found that the concentration of $O_2^{•-}$ showed a gradual decreasing when the reaction proceeded up to 1 min, which further corroborated the system $O_2^{•-}$ was intermediate for the $^1O_2$ generation (Fig. S13). Proton promoted $O_2^{•-}$ denitrification was one of the pathways for $^1O_2$ production [48]. The ability to significantly reduce the signal intensity of both DMPO-$O_2^{•-}$ and TEMP-$^1O_2$ by addition of p-BQ (Fig. S14) suggested that $O_2^{•-}$ was a key intermediate in the generation of $^1O_2$ again. Herein, the electron transfer process (ETP) and high valent metal effect were excluded based on the result (Text S8) from pre-mixing experiments (for ETP, Fig. S15), methyl phenyl sulfone ($PMSO_2$) transformation (for Fe(VI), Fig. S16) and periodate colorimetric method (for Cu(III), Fig. S17).

In conclusion, the CuS@Fe-CCBC/PMS system could produce •OH, $SO_4^{•-}$, $^1O_2$, and $O_2^{•-}$. Considering that $O_2^{•-}$ was an intermediate for the production of $^1O_2$, the producing concentration of which was difficult to be captured and quantified, so quantitative experiments were conducted to quantify the producing concentrations of the remaining three ROSs mentioned above. The results showed that the most ROSs were generated in the CuS@Fe-CCBC/PMS system compared to the CCBC, Fe-CCBC, CuS and CuS@CCBC activated PMS systems (Fig. S18). 3.84 μM, 1.74 μM and 11.57 μM were generated after 40 min for •OH, $SO_4^{•-}$ and $^1O_2$, respectively [49–51]. To further quantify the contribution of various ROSs on SMR removal, nitrobenzene (NB), benzoic acid (BA), and furfuryl alcohol (FFA in MeOH) were chosen as competition compounds for •OH, $SO_4^{•-}$ and $^1O_2$ to conduct probe experiments (Fig. S19, Fig. 4e). The steady-state concentrations of [•OH]ss, [$SO_4^{•-}$]ss, and [$^1O_2$]ss were calculated as 5.15 × 10^{-14} M, 5.64 × 10^{-15} M, and 1.58 × 10^{-11} M (Fig. 4f). The specific contribution rate of •OH, $SO_4^{•-}$, $^1O_2$, and $O_2^{•-}$ were further calculated as 28.1 %, 20.5 %, 46.7 % and 4.8 %, respectively (Fig. 4f).

3.4. Intrinsic mechanisms of PMS activation

3.4.1. Electron transfer mechanism in CuS@Fe-CCBC/PMS system

To elucidate the formation mechanism of ROSs, we systematically investigated the electron transfer processes from CuS@Fe-CCBC to PMS and SMR. The solid EPR analysis revealed the strongest characteristic signal of sulfur vacancies (S_v, g = 2.004) on the surfaces of CuS@Fe-CCBC (Fig. 5a) [52–54], which promoted selective cleavage of O—O bonds in PMS and direct ROSs formation pathways toward predominantly $^1O_2$ generation [55,56]. The concentration of S_v in all the samples was quantified by comparison with the total spin number and concentration of the standards and was summarized in Table S5. It could be seen that the total spin numbers were ranked from the smallest to the largest as Fe-CCBC (3.292 × 10^{17}), CuS (6.093 × 10^{17}), CuS@CCBC (7.832 × 10^{17}) and CuS@Fe-CCBC (8.192 × 10^{17}). This was mainly ascribed to the oxygen-rich functional groups on BC surfaces facilitated CuS nucleation and growth while promoting defect formation through metal coordination during Fe doping. Furthermore, Fe incorporation enhanced local electron density and weakened Cu—S bonding, enabling preferential sulfur loss and vacancy generation during the rapid curing process [57].

The electron transfer properties and processes of the CuS@Fe-CCBC/PMS system were further investigated by electrochemical measurements. Electrochemical impedance spectroscopy (EIS, Fig. 5b) of multiple samples revealed that the insertion of Fe into CuS@CCBC significantly reduced resistance in electron transfer process. CuS@Fe-CCBC could offer faster electron transfer to PMS and SMR with its greatest electron transport ability [58]. Based on the EIS detection results, an equivalent circuit diagram (Fig. S20) was fitted. Among them,

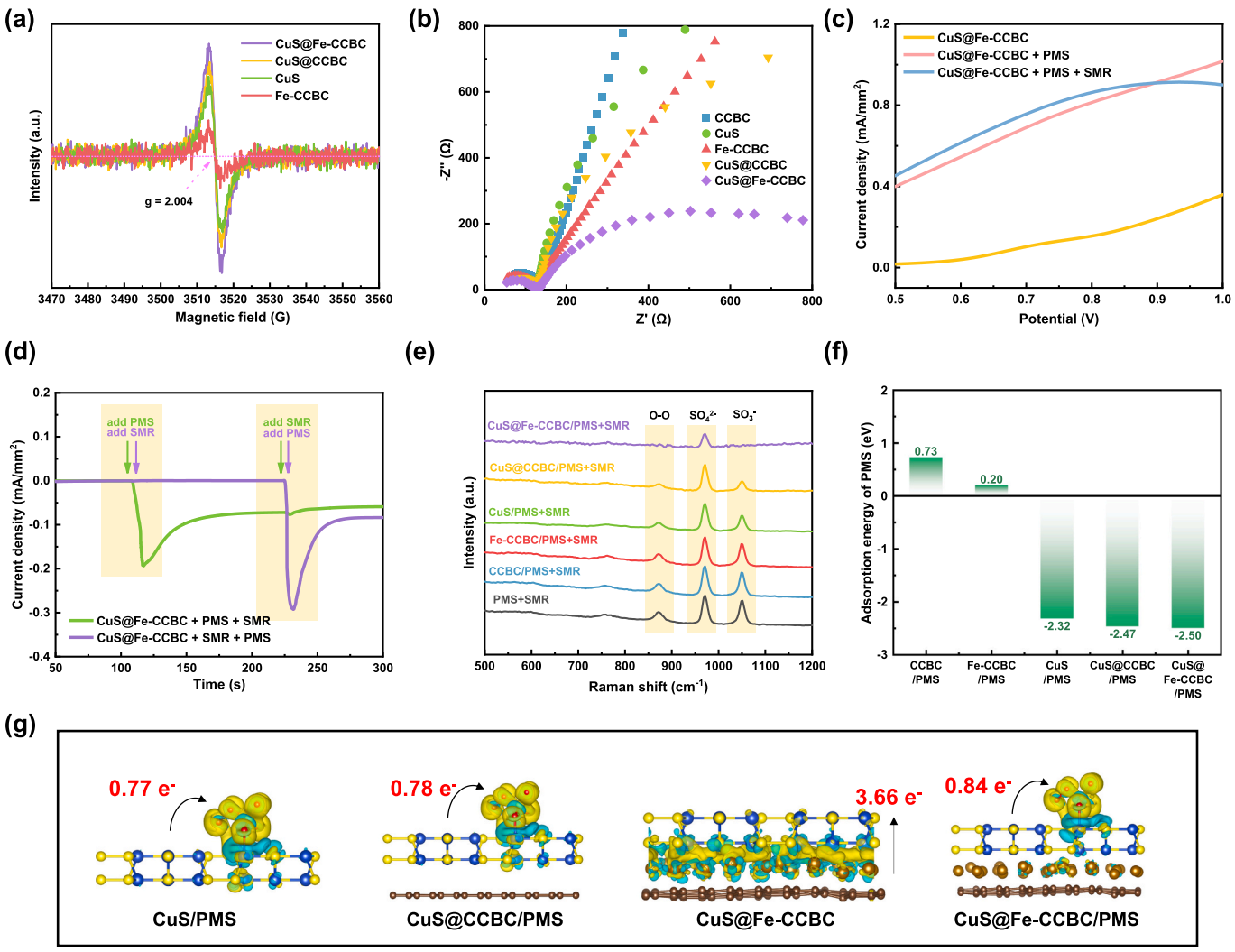

Fig. 5. (a) EPR spectra, (b) EIS Nyquist plots, (c) LSV curves, (d) i-t curves, (e) *in-situ* Raman spectra, (f) the adsorption energy of PMS and (g) differential charge density plots (blue region means electron depletion and yellow region means electron accumulation) with bader charges analysis in different system.

the R_{ct} values (Table S6), which represented the charge transfer resistance of the electrodes, were 84.9 Ω·cm^2 for CCBC, 82.3 Ω·cm^2 for Fe-CCBC, 72.5 Ω·cm^2 for CuS, 50.6 Ω·cm^2 for CuS@CCBC and 43.8 Ω·cm^2 for CuS@Fe-CCBC in descending order, indicating that the introduction of interfacial Fe nanodots reduced the resistance to electron transfer between the composite components. Linear voltammetry tests (LSV) elucidated the important role of metal Fe doping for CuS@CCBC in PMS activation. As shown in Fig. S21a, the CuS@Fe-CCBC exhibited much higher current density compared to CCBC, Fe-CCBC, CuS and CuS@CCBC, proving its greater reduction capability [2]. In addition, a significant increase in current density occurred by the addition of PMS in *in-situ* LSV test (Fig. 5c), suggesting that an oxidation reaction on the surface of CuS@Fe-CCBC, leading to a more efficient transfer of electrons to PMS and enhanced PMS decomposition. When SMR was dosed then, the current density did not increase further, confirming that the degradation of SMR did not rely on the transfer of electrons on the catalyst surface, but was oxidized by the ROSs in solution [59]. The cyclic voltammetry (CV) curves demonstrated that CuS@Fe-CCBC presented a greater current density and stronger reduction capacity (Fig. S21b). The two reduction peaks at −0.15 V, 0.07 V and the two oxidation peaks at 0.47 V, 0.65 V were attributed to the dual active centers of Fe^{2+}/Fe^{3+} and Cu^{+}/Cu^{2+}, which endowed the high activity of CuS@Fe-CCBC for PMS activation. The Tafel curves of several catalysts displayed (Fig. S21c) that CuS@Fe-CCBC possessed the smallest slope and exhibited the narrowest margin, indicating faster electron transfer rate and higher reactivity [2]. The larger curve intercept of CuS@Fe-CCBC implied the reductivity of which with PMS activation [60]. Therefore, the Fe-mediated electron bridge was successfully constructed in the CuS@Fe-CCBC to provide a rapid and smooth electron transfer process on the activation of PMS. The electrochemical active surface area (ECSA) of CuS@Fe-CCBC was further evaluated. The corresponding C_{dl} values were derived from the CV curves obtained at different scanning rates (Fig. S22a), and their values were calculated as 157 mF/cm^2 (Fig. S22b). This indicated that the high exposure of effective active sites accelerated the catalytic process in the CuS@Fe-CCBC heterojunction structure [61].

3.4.2. *Enhanced mechanisms for PMS decomposition*

As noticed in *in-situ* chronoamperometric curves (Fig. 5d), the first addition of SMR did not result in current changes, indicating that the contaminant removal process did not depend on adsorption and ETP [62]. With the introduction of PMS afterwards, a significant negative current was generated, proving the rapid decomposition of PMS on CuS@Fe-CCBC, while SMR did not occupy the active sites. When PMS was introduced first, the current of CuS@Fe-CCBC showed obvious fluctuations. Apparently, the presence or absence of contaminants would not affect the adsorption and decomposition of PMS. However, the intensity of this current change was lower than that in the case of

coexistence with SMR, which was mainly due to the enhanced PMS activation caused by the consumption of ROSs by SMR [59].

To elucidate PMS decomposition during catalytic activation for SMR degradation, we conducted *in-situ* Raman analysis of PMS electronic structure evolution across systems after 40 min reaction (Fig. 5e). Control measurements with PMS/SMR mixtures revealed characteristic vibrational modes: O—O (HSO_5^-, 890 cm^{-1}), SO_4^{2-} (983 cm^{-1}) and SO_3^- (S—O, 1159 cm^{-1}) [63]. Compared to CCBC/PMS and Fe-CCBC/PMS systems, CuS-containing systems (CuS/PMS and CuS@CCBC/PMS) attenuated HSO_5^- peaks, indicating electron transfer from CuS to PMS that enabled HSO_5^- consumption for ROSs-dominant SMR degradation. Crucially, the CuS@Fe-CCBC/PMS system achieved complete PMS decomposition, with near-disappearance of O—O and SO_3^- signals, demonstrating that CuS@Fe-CCBC initiated rapid electron transfer to form CuS@Fe-CCBC-PMS* complexes, followed by sustained electron assault on HSO_5^- through redox cycling [64–66]. In order to further clarify the changes of O—O and S—O bonds during the activation of PMS by CuS@Fe-CCBC, the changes of the electronic structure of PMS with reaction time were investigated using *in-situ* Raman. As shown in Fig. S23, compared with the electronic structure of pristine PMS, both the O—O peak at 890 cm^{-1} and S—O peak at 1159 cm^{-1} were weakened with the increase of the reaction time after the addition of CuS@Fe-CCBC, and finally disappeared completely after 40 min. This further suggested that the activation of PMS by CuS@Fe-CCBC mainly broke its O—O and S—O bonds to generate ROSs for pollutant degradation.

To simplify density functional theory (DFT) calculations, a substrate composed of C atoms was used to represent CCBC [29]. The electronic density distributions of various catalysts in Fig. S24 showed that the introduction of Fe nanodots into the CuS@CCBC interval produced a larger electron density region in the CuS@Fe-CCBC composite. The high electron density region indicated that Fe nanodots acted as an electronic bridge making CuS@Fe-CCBC more active in electron transfer [67]. In addition, the electron localization function (ELF) distribution of the catalysts Fig. S25 further showed that electron delocalization and localization coexisted in the CuS@Fe-CCBC structure. It suggested that the interfacial Fe nanodots constructed an electron transfer channel between the CuS and CCBC layers for promoting further electron transfer [68].

As shown in Fig. 5f, PMS adsorption on CCBC and Fe-CCBC surfaces was thermodynamically unfavorable. For CuS (−2.32 eV), CuS@CCBC (−2.47 eV) and CuS@Fe-CCBC (−2.50 eV), the adsorption energy of PMS on the catalyst surface was gradually enhanced. This indicated that the coexistence of CuS and Fe made PMS more easily to be activated (the corresponding adsorption configurations were provided in Fig. S26). It corresponded to the experimental results where CuS@Fe-CCBC showed the best decomposition of PMS before. However, compared to CuS (1.476 Å) and CuS@CCBC (1.479 Å), CuS@Fe-CCBC (1.474 Å) did not exhibit stretching of O—O bonds in PMS (Fig. S27). That meant that the co-exitance of CuS and Fe did not contribute much to the facilitation of the electron transfer process that took place in the antibonding orbitals of O—O. As we observed in *in-situ* Raman result, the synergistic promotion was more focused on the S—O bond breaking process, which was the main factor in the generation of $^1O_2$ [69]. This also corresponded to the dominance of $^1O_2$ in the CuS@Fe-CCBC/PMS system. Fig. 5g illustrated the differential charge density in different system, where the blue region meant electron depletion and the yellow region meant electron accumulation. Based on the bader charge analysis, it was Fe intercalation that allowed more electrons transfer from the Fe-CCBC substrate to CuS (3.66 e^-, cumulative number of electrons transferred in fixed fragment) compared with that in CuS@CCBC without Fe nanodots (0.28 e^- in Fig. S28), which was also proved by the EIS results of catalysts. Subsequently, more electron transfer (0.84 e^-) was indeed occurred between PMS and CuS@Fe-CCBC. The experimental and theoretical results indicated that optimal adsorption and decomposition processes of PMS on the CuS@Fe-CCBC surface were attributed to the facilitation on internal electron transfer by the interfacial Fe nanodots.

3.4.3. Dual redox sites mechanism for PMS activation

Based on the above synergistic effect of CuS and metal Fe on CCBC, the elemental chemical valence states of the catalysts before and after the reaction were further explored *via* the X-ray photoelectron spectroscopy (XPS) (Fig. 6, Table S7). It was found that the elemental composition of CuS@Fe-CCBC did not change after the reaction (Fig. 6a). As observed in C 1s and O 1s spectrum (Fig. 6b and c), CuS@Fe-CCBC showed a shift from C═O to C—O, illustrating the conversion acted as electron acceptor interacting with PMS and the generation of $^1O_2$ [10]. As shown in Fig. 6d, the percentage of Fe^{2+} on the surface of used CuS@Fe-CCBC decreased from 66.95 % to 56.89 %, correspondingly the percentage of Fe^{3+} increased from 33.05 % to 43.11 %, compared with that of fresh CuS@Fe-CCBC. This suggested that elemental Fe was involved in the redox reaction of activated PMS, and the transition from low to high valence states thermodynamically triggered the decomposition of PMS into $SO_4^{\bullet-}$ and •OH (Eqs. (1)–(2)) [70]. Subsequently, $SO_4^{\bullet-}$ could be further hydrolyzed to form •OH (Eq. (3)). The low-valent copper (Cu^+) could be the main active site for electron transfer to PMS, forming Cu^{2+} during PMS activation (Eqs. (4)–(5)) as well. Moreover, thermodynamically followed E_0 (Cu^+/Cu^{2+}) = (0.38 V) < E_0 (Fe^{3+}/Fe^{2+}) = (0.77 V), elemental Cu and Fe could realize internal redox cyclic transformation (Eq. (6)). However, as displayed in Fig. 6e, the percentage of low-valent Cu^+ on the catalyst surface further increased after the reaction, confirming the presence of another booster to accelerate the oxidative cycling reaction of Cu^+/Cu^{2+} in the CuS@Fe-CCBC/PMS system. Based on the evolution of the reduced S^{2-} fraction on the CuS@Fe-CCBC surface, it was found (Fig. 6f) that the percentages of S^{2-} and S_2^{2-} decreased by 12.44 % and 1.1 % after used, while S_n^{2-} and SO_4^{2-} increased by 11.01 % and 2.62 %. This indicated that during the activation of PMS by CuS@Fe-CCBC, S^{2-} and S_2^{2-} acted as electron donors and regenerated Fe^{2+} and Cu^+ during their conversion to S_n^{2-} and SO_4^{2-}, further achieving the high activity of CuS@Fe-CCBC (Eqs. (7)–(10)) [13,27].

To further verify the existence of double redox cycles (Fe^{2+}/Fe^{3+}, Cu^+/Cu^{2+}) in the PMS activation process with CuS@Fe-CCBC, Fe^{3+} and Cu^{2+} were introduced into the CuS@Fe-CCBC/PMS system, respectively. As shown in Fig. S29a, the degradation rate of SMR was significantly accelerated with the increase of Fe^{3+} injection concentration, whereas the homogeneous Fe^{3+}/PMS system could hardly degrade SMR. This demonstrated the existence of other oxidation cycle pairs as an electron donor in CuS@Fe-CCBC, which was able to promote the Fe^{2+}/Fe^{3+} redox cycle during the activation of PMS [71]. In Fig. S29b, the addition of Cu^{2+} played an inhibitory role in the degradation of SMR in the CuS@Fe-CCBC/PMS system, which implied that too much Cu^{2+} could not provide electrons for the regeneration of Fe^{2+}, limiting the running of the redox cycle. Herein, the dual redox sites, mainly Fe^{2+}/Fe^{3+} and Cu^+/Cu^{2+}, were further confirmed.

As mentioned earlier, the $^1O_2$ in the system may be generated indirectly *via* $O_2^{\bullet-}$. Specifically, when PMS was added to the system, the current density of the CuS@Fe-CCBC working electrode increased significantly (Fig. 5d), indicating the transfer of electrons from PMS to the surface of CuS@Fe-CCBC, accompanied by the generation of $O_2^{\bullet-}$. $O_2^{\bullet-}$ reacted with H_2O in a series of complex reactions to generate $^1O_2$ (Eqs. (11)–(13)) [12,48]. The reaction between $SO_5^{\bullet-}$ and H_2O was also another pathway for $^1O_2$ production (Eqs. (14)–(16)). In addition, self-dissociation of PMS could also form $^1O_2$ (Eq. (17)). In summary, the possible mechanism of PMS activation by dual redox sites in CuS@Fe-CCBC was shown in Fig. 6g, and the final mineralization of SMR was achieved by the multiple ROSs (•OH, $SO_4^{\bullet-}$ and $^1O_2$) in the CuS@Fe-CCBC/PMS system (Eq. (18)).

$$Fe^{2+} + HSO_5^- \rightarrow Fe^{3+} + SO_4^{\cdot-} + OH^- \quad (1)$$

$$Fe^{2+} + HSO_5^- \rightarrow Fe^{3+} + SO_4^{2-} + \dot{O}H \quad (2)$$

$$SO_4^{\cdot-} + H_2O \rightarrow SO_4^{2-} + H^+ + \dot{O}H \quad (3)$$

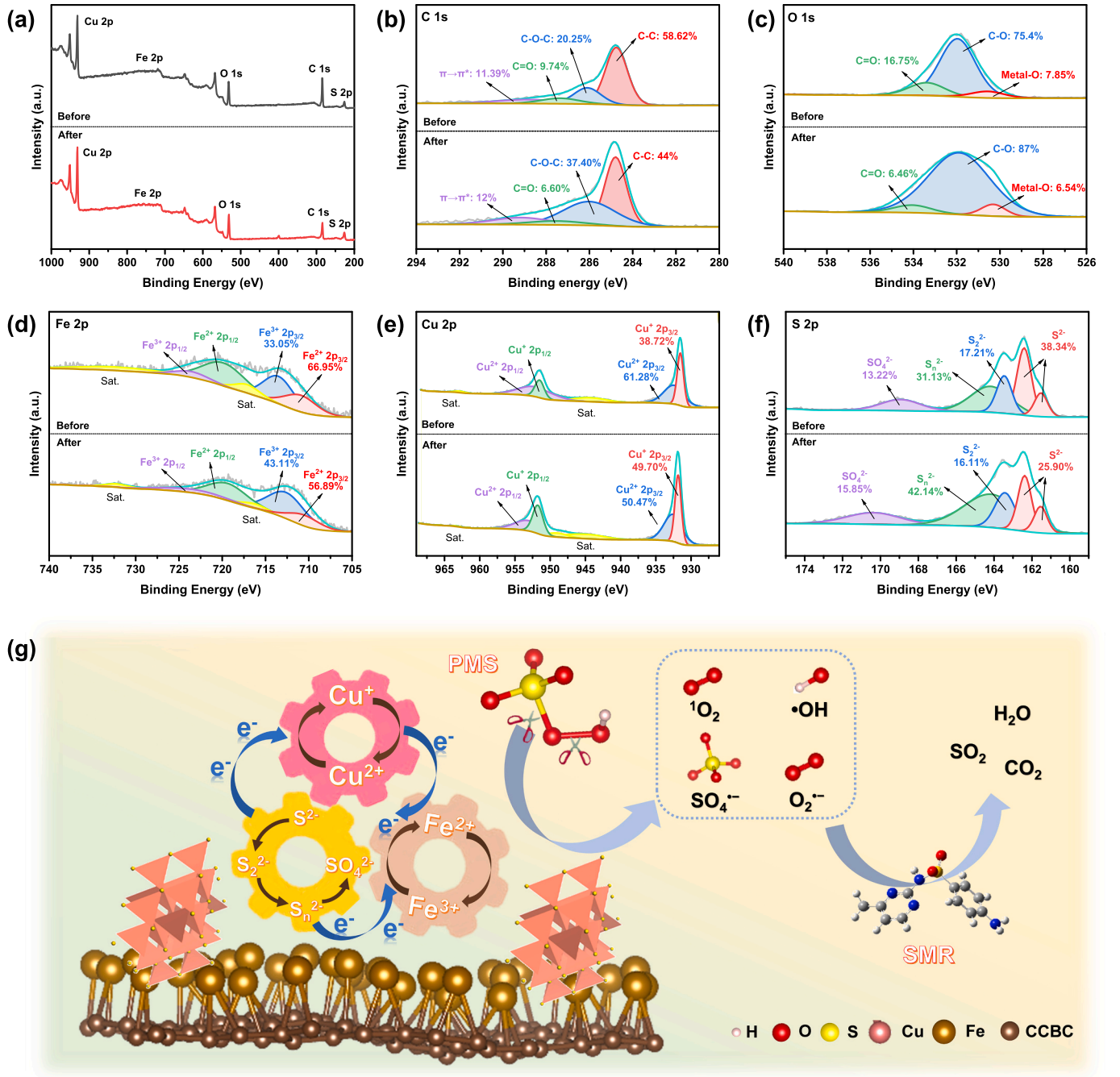

Fig. 6. XPS spectra of CuS@Fe-CCBC before and after use: (a) survey spectra, (b) C 1s, (c) O 1s, (d) Fe 2p, (e) Cu 2p and (f) S 2p. (g) The proposed mechanism scheme of SMR removal in the system of CuS@Fe-CCBC/PMS.

$$Cu^{+} + HSO_5^- \rightarrow Cu^{2+} + SO_4^{\cdot-} + OH^- \quad (4)$$

$$Cu^{+} + HSO_5^- \rightarrow Cu^{2+} + SO_4^{2-} + \dot{O}H \quad (5)$$

$$Cu^{+} + Fe^{3+} \rightarrow Cu^{2+} + Fe^{2+} \quad (6)$$

$$2S^{2-} + 2Cu^{2+}(Fe^{3+}) \rightarrow 2Cu^{+}(Fe^{2+}) + S_2^{2-} \quad (7)$$

$$nS_2^{2-} + 2(n-2)Cu^{2+}(Fe^{3+}) \rightarrow 2(n-2)Cu^{+}(Fe^{2+}) + 2S_n^{2-} \quad (8)$$

$$S_n^{2-} + 2Cu^{2+}(Fe^{3+}) \rightarrow 2Cu^{+}(Fe^{2+}) + nS^0 \quad (9)$$

$$S^0 + Cu^{2+}(Fe^{3+}) \rightarrow Cu^{+}(Fe^{2+}) + SO_4^{2-} \quad (10)$$

$$Cu^{2+} + 2HSO_5^- \rightarrow Cu^{+} + 2SO_4^{2-} + 2H^+ + O_2^{\cdot-} \quad (11)$$

$$O_2^{\cdot-} + H_2O \rightarrow HOO^{\cdot} + OH^- \quad (12)$$

$$O_2^{\cdot-} + HOO^{\cdot} \rightarrow HOO^- + {}^1O_2 \quad (13)$$

$$Fe^{3+} + HSO_5^- \rightarrow Fe^{2+} + SO_5^{\cdot-} + H^+ \quad (14)$$

$$Cu^{2+} + HSO_5^- \rightarrow Cu^{+} + SO_5^{\cdot-} + H^+ \quad (15)$$

$$4SO_5^{\cdot-} + 2H_2O \rightarrow 4HSO_4^- + SO_4^{2-} + {}^1O_2 \quad (16)$$

$$HSO_5^- + HSO_5^- \rightarrow HSO_4^- + SO_4^{2-} + H^+ + {}^1O_2 \quad (17)$$

$$OH/SO_4^{\cdot-}/{}^1O_2 + SMR \rightarrow CO_2 + SO_2 + H_2O \quad (18)$$

3.5. Proposed degradation pathways of SMR

This study employed density functional theory (DFT) calculations to theoretically predict potential reactive sites for active species attacking SMR (Fig. 7a1). According to frontier molecular orbital theory, the highest occupied molecular orbital (HOMO) possessed the high electron energy and weak binding force, facilitating electron escape and consequently exhibiting higher susceptibility to electrophilic attack. The predominant ROSs (•OH, $SO_4^{\cdot-}$ and $^1O_2$) in the CuS@Fe-CCBC/PMS system were recognized as electrophilic species [72]. As shown in the HOMO diagram of SMR (Fig. 7a2), the N7, C8, C11, C12, and C13 positions with larger isosurface volumes were identified as potential electrophilic attack sites. The electrostatic potential distribution (ESP) of SMR (Fig. 7a3) revealed that besides the aforementioned positions, the central —SO_2— group also existed as potential reactive sites, as electrophilic species preferentially attacked regions with high negative electrostatic potentials [73]. To further elucidate the susceptibility of individual atoms to electrophilic attack, Fukui function indexes were analyzed. Hirschfeld charge calculations demonstrated that the condensed f^- values for N7 (0.1828), C8 (0.0894), C11 (0.0717), C12 (0.0876), and C13 (0.0948) significantly surpassed those of other atoms (Fig. 7a4), indicating these atoms owned enhanced reactivity and were more prone to be electrophilic attacked by ROSs.

The intermediates of SMR in the CuS@Fe-CCBC/PMS system were examined by liquid chromatograph mass spectrometer/mass spectrometer (LC-MS/MS), and a total of 12 intermediates were detected (Fig. S30, Table S8). Accordingly, three possible degradation pathways of SMR ($C_{11}H_{12}N_4O_2S$, m/z = 265) were proposed (Fig. 7b, Text S9): I) substitution of hydrogen on the amino group by •OH attack; II) extruded rearrangement of SO_2 and III) breakage of —S—C—, —S—N— chemical bonds. SMR was undetectable in the HPLC at the end of the reaction, but based on the TOC removal rate of 41.3 %, it indicated that 41.3 % of SMR was mineralized into inorganic matter such as SO_2, CO_2 and H_2O, and the remaining 58.7 % existed in the system as non-toxic small molecule organic matter, like P9, P10, P11, P12.

To comprehensively assess the toxicity of SMR degradation intermediates, quantitative structure-activity relationship (QSAR) analysis was performed using the Toxicity Estimation Software Tool (T.E.S.T.), evaluating four critical toxicity indicators: acute toxicity (rat oral LD_{50}), bioaccumulation factor, developmental toxicity, and mutagenicity (MG) values. Notably, certain intermediates exhibited higher

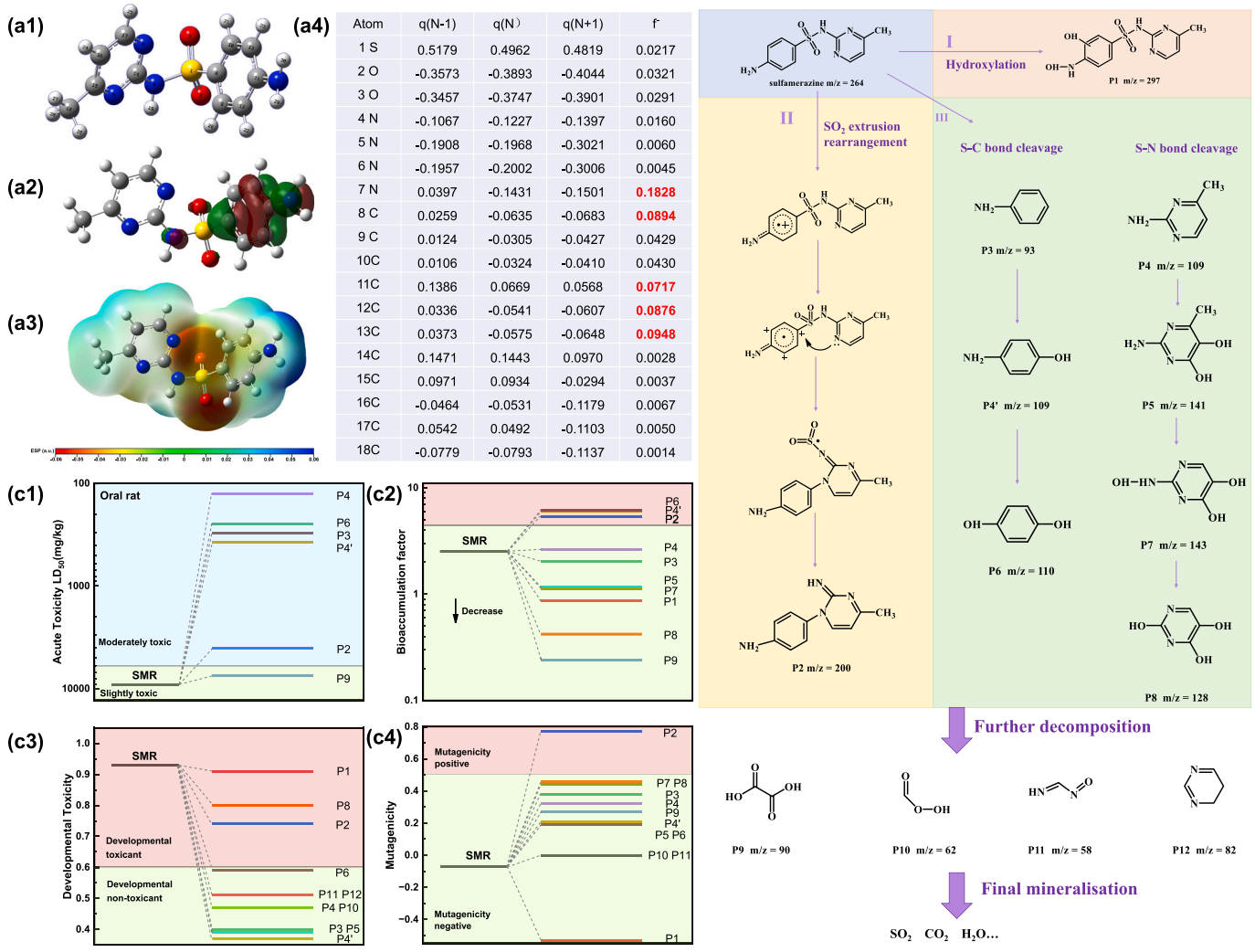

Fig. 7. (a) 1: Optimized molecular structure, 2: HOMO, 3: electrostatic potential (ESP) distribution and 4: natural population analysis (NPA) charge distribution and reduced Fukui index (f^-) of SMR. (b) The proposed degradation pathway of SMR in the CuS@Fe-CCBC/PMS system. (c) Toxicity prediction of SMR and corresponding intermediates, 1: acute toxicity (oral rat LD_{50}), 2: bioaccumulation factor, 3: developmental toxicity and 4: mutagenicity.

acute toxicity (oral LD_{50}) than the parent SMR in rat models (Fig. 7c1). Most intermediates demonstrated reduced bioaccumulation potential compared to SMR (Fig. 7c2), while all degradation products showed diminished developmental toxicity relative to the parent compound (Fig. 7c3). Particularly, the majority of intermediates were classified as non-mutagenicity toxicants (Fig. 7c4). Collectively, these results indicated that the CuS@Fe-CCBC/PMS system effectively reduced the overall toxicity of SMR through catalytic degradation [1,9].

3.6. Application of CuS@Fe-CCBC/PMS in continuous-flow reactor

The effects of coexisting anions (Cl^-, NO_3^-, HCO_3^- and HPO_4^{2-}) and natural organic matter (NOM) in water on SMR degradation were investigated to assess the complex environmental adaptability of the novel CuS@Fe-CCBC. The specific phenomena and reasons were detailed in Fig. S31a–e, Text S10. In conclusion, the CuS@Fe-CCBC/PMS system has great adaptability to complex environments. As depicted in Fig. S31f, the CuS@Fe-CCBC/PMS system was able to maintain excellent degradation in actual water matrix, including tap water, Qinghe river and secondary effluent from a wastewater treatment plant (WWPT) (Table S9 offered the main water quality parameters).

The deep purification potential of the CuS@Fe-CCBC/PMS system for advanced treatment of wastewater treatment plant (WWTP) secondary effluent were systematically evaluated. 3D excitation-emission-matrix

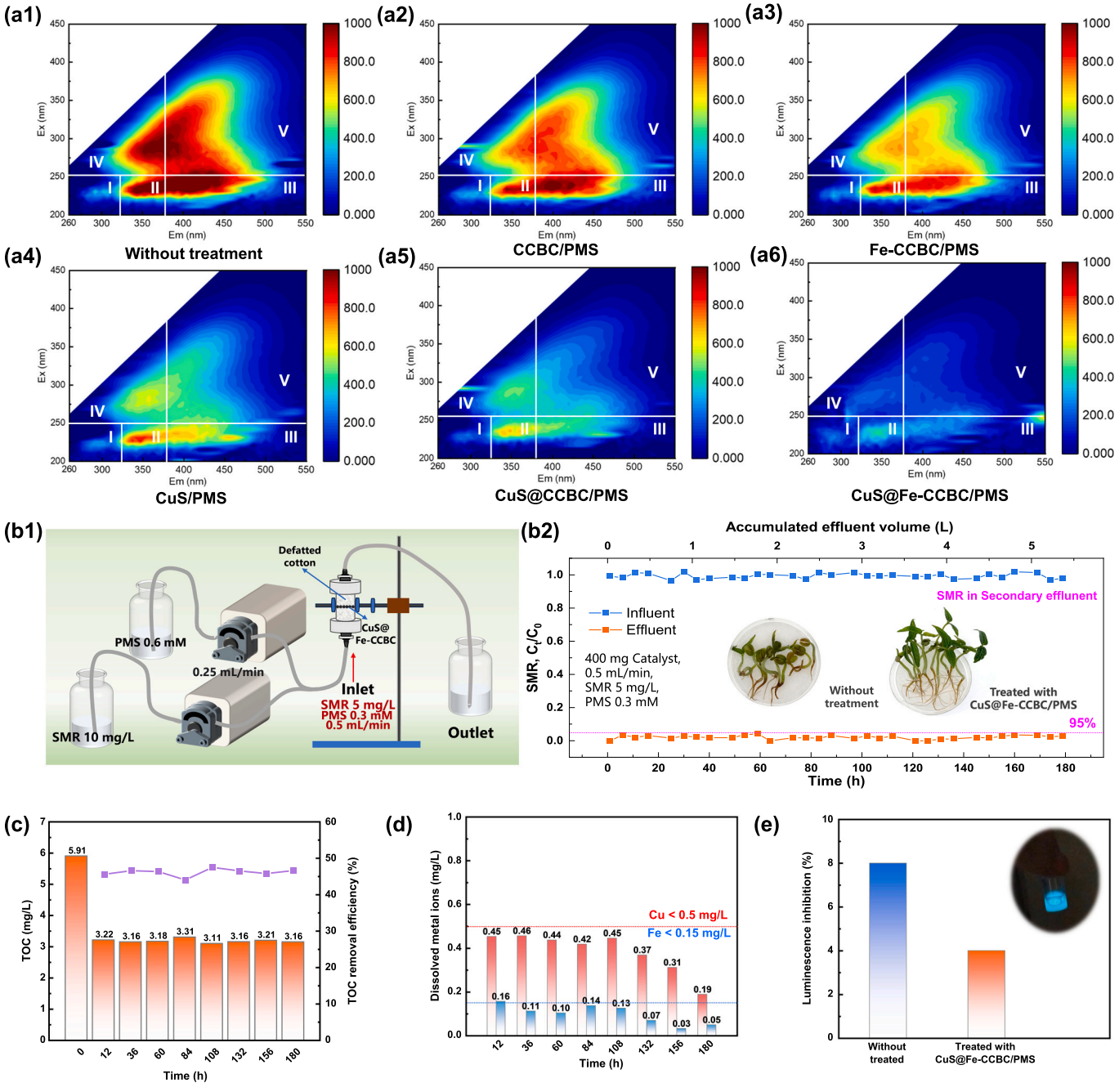

Fig. 8. (a) Fluorescence EEM spectra of the secondary effluent from WWPT treated with different system. (b1) Schematic illustration continuous-flow device. (b2) SMR degradation efficiency (inset: influence of influent and effluent on the growth of *bean sprouts*), (c) TOC change and removal rate during 180 h by the continuous-flow treatment. (d) The metal leaching in the effluent every day. (e) Luminescence inhibition effect on the *Vibrio fischeri* (Inset: its Optical image) before and after the continuous-flow treatment. Experiments conditions: $[PMS]_0$ = 0.3 mM, $[Catalyst]_0$ = 100 mg/L, T = 25 °C, and initial pH = 5.57.

(EEM) spectra analysis revealed that secondary effluent, characterized by aromatic protein (Region II), fulvic acid (Region III), soluble microbial byproducts (Region IV) and humic substances (Region V) (Fig. 8a1), achieved substantial purification within 40 min (Fig. 8a6). Comparative analysis demonstrated the superior performance of the synergistic CuS@Fe-CCBC/PMS system, exhibiting greater fluorescence intensity reduction than CCBC/PMS (Fig. 8a2), Fe-CCBC/PMS (Fig. 8a3), CuS/PMS (Fig. 8a4) and CuS@CCBC/PMS (Fig. 8a5) systems. The optimal system realized 46.0 % mineralization efficiency, reducing TOC from 3.304 mg/L to 1.837 mg/L (Fig. S32a). Furthermore, UV_{254} absorbance, indicative of humic macromolecules and conjugated aromatic structures decreased by 50.6 % within 40-min reaction (Fig. S32b), confirming effective degradation of complex organic compounds.

A continuous-flow reactor was constructed to further investigate the long-term operational effects of CuS@CCBC/PMS for the degradation of SMR in real water. As shown in Fig. 8b1, the concentration-doubled PMS and SMR solutions were passed through a continuous-flow reaction column with a volume of about 21 mL at a flow rate of 0.25 mL/min (total flow rate of 0.5 mL/min, HRT = 40 min). Fig. S33 and Text S11 demonstrated the effectiveness of the continuous-flow reactor for treating SMR in the Qinghe river. Then, as illustrated in Fig. 8b2, the SMR removal rate in the secondary effluent was consistently above 95 % with an average mineralization rate of 46.1 % after 180 h (7.5 d) of continuous operation (Fig. 8c), indicating the long-lasting stability of CuS@Fe-CCBC/PMS in treating wastewater. In addition, the metal ions in the final effluent were all under the standard limits of Cu below 0.5 mg/L (GB 18918-2002) and Fe below 0.3 mg/L (GB 3838-2002) in China (Fig. 8d), and the consumption rate of PMS was guaranteed to be more than 90 % during this period (Fig. S34a). Benefiting from the good buffering performance of the secondary effluent which was mainly attributed to the CO_3^- (HCO_3^-) ions in it (pKa = 10.33) [74,75]. The pH of the effluent was also controlled between 6 and 9 (Fig. S34b), indicating that no additional secondary pollution was introduced by this continuous-flow operation process. Based on the luminescent bacteria inhibition experiments, it was found that the luminescence inhibiting rate of *Vibrio fischeri* was significantly reduced after treatment (Fig. 8e). Combined with the germination of *aquatic bean sprouts*, it was found that the *bean sprouts* watered with treated effluent water grew well, whose total rhizome length reached 8 cm, which was significantly better than that of the *bean sprouts* watered with raw water (5 cm) (Fig. S35). This proved that the continuous-flow treatment process was a toxicity reduction process. The above findings comprehensively confirmed the durability and feasibility of CuS@Fe-CCBC/PMS continuous deep treatment of secondary effluent, highlighting its great potential for practical application.

After using for 180 h, a series of characterizations of CuS@Fe-CCBC revealed that the structure of the biochar layer of CuS@Fe-CCBC had collapsed to a certain extent (Fig. S36a), the exposed metal Fe active species were heavily depleted (Fig. S36b). Depending on the results of elemental content of CuS@Fe-CCBC before and after 180-h continuous-flow running (Table S10), The change in CuS fraction was almost negligible, but some reduction in the content of iron species occurred, which was consistent with the XRD results. From FTIR spectra (Fig. S37), the hydroxyl groups adsorbed on the surface of CuS@Fe@CCBC after 180-h usage were significantly reduced, which may be one of the important reasons for the deactivation of the catalyst in the future [76,77]. At the same time, the C═C and C═O bonds underwent a shift to C—O bonds, which was consistent with the previous XPS results (Fig. 6b and c), indicating a large amount of $^1O_2$ production during the process. It was noteworthy that the Fe—O structure near ~612 cm^{-1} was observed here, which might be a product of the gradual deactivation of the catalyst [37]. Based on the XPS results, the inclusion of C 1s, O 1s, Fe 2p, Cu 2p and S 2p in used CuS@Fe-CCBC did not change by full spectra (Fig. S38a). The slight changes of C1s and O1s (Fig. S38b and c) offered no significant effect on catalytic reaction. From Fig. S38d, the area of Fe^{2+} decreased from 66.95 % to 44.59 %, which was consumed more than single batch reaction (56.89 %). As for Cu^+, instead of a further increase of percentage like single batch reaction (49.70 %), there was a little slight decrease (from 38.72 % to 38.27 %) in From Fig. S38e. It could be further demonstrated that the Fe^{2+} and Cu^+ contents, which played a major role in the decomposition of PMS, have undergone a certain degree of reduction. Notably, although no sustained regeneration of Fe^{2+} and Cu^+ was found after using for 180 h, it could not deny that the S species still provided electrons for their regeneration as electron donors, leading to the generation of S_2^{2-} (from 17.21 % to 21.72 %) and SO_4^{2-} (from 13.22 % to 16.68 %) (Fig. S38f). The problem of gradual failure of effective active site regeneration is inevitable in continuous-flow running thereafter. However, based on the ultra-simple synthesis idea of CuS@Fe-CCBC, the active components of the material can be regenerated using Na_2S solution continuously passing through the reaction column to prolong its use [78].

In order to further explore the application potential of CuS@Fe-CCBC/PMS in the most realistic situation, the tail water of a pharmaceutical wastewater treatment plant was taken and treated in depth (its water quality parameters offered in Table S9). The results showed that the chemical oxygen demand (COD) value of the tail effluent further decreased by 41.1 % after 3-h deep treatment when PMS and catalyst were dosed at 1 mM and 0.3 g/L (Fig. S39). In short, the CuS@Fe-CCBC catalyst was of industrialization potential, which was mainly attributed to the low-cost “rapid grinding” CuS loading process; the possibility of *in-situ* regeneration of the catalyst; and the ability to match the mainstream processes (*e.g.*, CAST, A^2/O) for integrating applications to achieve the deep purification of the secondary effluent.

4. Conclusions

CuS@Fe-CCBC composites were prepared by rapid grinding CuS on CCBC with interfacial Fe nanodots. This CuS@Fe-CCBC/PMS system activated PMS of nearly 100 % in 40 min to achieve complete degradation of SMR (k_{obs} = 0.082 min^{-1}). Meanwhile, the effects of loading ratio, PMS concentration, pH value, and cyclic use on the degradation effect were comprehensively investigated. The major ROSs (•OH, $SO_4^{\bullet-}$, $^1O_2$, and $O_2^{\bullet-}$) and their contributions (28.1 %, 20.5 %, 46.7 % and 4.8 %) in the CuS@Fe-CCBC/PMS system were determined by quenching experiments, EPR assays and probe tests. Based on electrochemical, *in-situ* Raman and XPS results, it was confirmed that the dual active centers of Cu^+/Cu^{2+} and Fe^{2+}/Fe^{3+} facilitated by S^{2-} could consistently deliver electrons to PMS. With DFT calculation analysis, the adsorption and activation of PMS on the surface of CuS@Fe-CCBC were more favorable due to Fe-mediated electron bridge between CuS and CCBC. Moreover, the CuS@Fe-CCBC/PMS system could deeply treat SMR-contained secondary effluent continuously (>95 %, 180 h) and reduce its toxicity. Based on the catalyst design ideas in this study, the use of a few metal nanodots as interlayer to promote electron migration and transfer between the composite catalyst components provided insights for the future development of PMS activators. Whether metals other than iron have the potential to construct electronic bridges, and whether the construction of electronic bridges is applicable to other carbon-based or metal-loaded materials are worth exploring in depth. In addition, when faced with the complex environment of real-world actual wastewater, AOPs capable of generating multiple ROSs were more environmentally resilient than systems targeted to generate a single ROS, which are worth obtaining more expand research. In summary, we provided an affordable and sustainable route for the effective treatment of antibiotic residues in wastewater.

CRediT authorship contribution statement

Xinyi Zhang: Writing – original draft, Validation, Data curation. **Jian Wei:** Writing – review & editing, Supervision. **Zhuang Guo:** Writing – review & editing, Funding acquisition, Conceptualization. **Liangjie Wang:** Writing – review & editing, Visualization. **Junfeng**

Dou: Resources, Investigation. **Yonghui Song:** Supervision, Funding acquisition.

Declaration of competing interest

The authors declare no conflict of interest.

Acknowledgments

This work was supported by National Key Research and Development Program of China (NO. 2021YFC3201505), National Natural Science Foundation of China (NO. 22206177) and China Postdoctoral Science Foundation (No. 2025M771279).

Appendix A. Supplementary data

Supplementary data to this article can be found online at https://doi.org/10.1016/j.cej.2025.166480.

Data availability

Data will be made available on request.

References

[1] Y. Guo, X. Zhu, Z. Guo, J. Wei, T. Hao, D. Xu, An innovative method to in-situ enhance activity of natual coal in peroxymonosulfate system: Activation of original components, Chem. Eng. J. 507 (2025) 160552.
[2] J. Liang, L. Fu, K. Gao, X. Duan, Accelerating radical generation from peroxymonosulfate by confined variable Co species toward ciprofloxacin mineralization: ROS quantification and mechanisms elucidation, Appl. Catal. Environ. 315 (2022) 121542.
[3] D. Cheng, H.H. Ngo, W. Guo, S.W. Chang, D.D. Nguyen, Y. Liu, Q. Wei, D. Wei, A critical review on antibiotics and hormones in swine wastewater: water pollution problems and control approaches, J. Hazard. Mater. 387 (2020) 121682.
[4] Z. Aversa, E.J. Atkinson, M.J. Schafer, R.N. Theiler, W.A. Rocca, M.J. Blaser, N. K. LeBrasseur, Association of infant antibiotic exposure with childhood health outcomes, Mayo Clin. Proc. 96 (2021) 66–77.
[5] Y. Lu, X. Zhou, Y. Zheng, H. Yang, W. Cao, How far do we still need to go with antibiotics in aquatic environments? Antibiotic occurrence, chemical-free or chemical-limited strategies, key challenges, and future perspectives, Water Res. 275 (2025) 123179.
[6] Y. Liu, M. Zhang, Y. Wu, S. Li, J. Hu, W. Sun, J. Ni, Profiles, drivers, and prioritization of antibiotics in China's major rivers, J. Hazard. Mater. 477 (2024) 135399.
[7] X. Yang, J. Duan, J. Qi, X. Li, J. Gao, Y. Liang, S. Li, T. Duan, W. Liu, Modulating the electron structure of Co-3d in $Co_3O_{4-x}/WO_{2.72}$ for boosting peroxymonosulfate activation and degradation of sulfamerazine: roles of high-valence W and rich oxygen vacancies, J. Hazard. Mater. 445 (2023) 130576.
[8] Q. Yuan, D. Zhang, P. Yu, R. Sun, H. Javed, G. Wu, P.J.J. Alvarez, Selective adsorption and photocatalytic degradation of extracellular antibiotic resistance genes by molecularly-imprinted graphitic carbon nitride, Environ. Sci. Technol. 54 (2020) 4621–4630.
[9] Y. Guo, Z. Guo, J. Wei, J. Zhang, Y. Huang, T. Hao, C. Wang, D. Xu, Iron anchored carbon-nitrogen catalyst for enhanced activation performance of peroxymonosulfate: synergy of $^1O_2$ and high-valent iron, Sep. Purif. Technol. 353 (2025) 128381.
[10] J. Sun, D. Zhang, D. Xia, Q. Li, Orange peels biochar doping with Fe-Cu bimetal for PMS activation on the degradation of bisphenol A: a synergy of $SO_4^{\bullet-}$, $^{\bullet}OH$, $^1O_2$ and electron transfer, Chem. Eng. J. 471 (2023) 144832.
[11] Y. Guan, G. Zhou, Y. Jiang, J. Dong, L. Li, J. Yin, S. Huang, L. Zhang, E.H. Ang, Lattice distortion effects in high-entropy oxides: boosting PMS activation for effective and durable pollutant degradation, Sep. Purif. Technol. 358 (2025) 130267.
[12] F. Wang, Y. Zhang, Y. Peng, W. Xiao, W. Yu, H. Wang, Z. Bian, Continuous peroxymonosufate activation for antibiotics degradation via fluorine-free-$Ti_3C_2T_x$-$CoFe_2O_4$ hydrogel beads: Performance, mechanism and application, Applied Catalysis B: Environment and Energy. 358 (2024) 124441.
[13] X. Zhang, Y. Gao, Y. Li, Y. Zhou, H. Ma, J. Shang, X. Cheng, Synthesis of magnetic $NiFe_2O_4$/CuS activator for degradation of lomefloxacin via the activation of peroxymonosulfate under simulated sunlight illumination, Sep. Purif. Technol. 288 (2022) 120664.
[14] X. Zhang, J. Wei, C. Wang, L. Wang, Z. Guo, Y. Song, Recent advance of Fe-based bimetallic persulfate activation catalysts for antibiotics removal: Performance, mechanism, contribution of the key ROSs and degradation pathways, Chem. Eng. J. 487 (2024) 150514.
[15] Y. Ding, L. Fu, X. Peng, M. Lei, C. Wang, J. Jiang, Copper catalysts for radical and nonradical persulfate based advanced oxidation processes: certainties and uncertainties, Chem. Eng. J. 427 (2022) 131776.
[16] X. Fu, L. Yan, H. Qi, W. Song, Y. Li, X. Li, Enhanced activation of peroxymonosulfate by CuO modified biochar through mechanochemical synthesis: insights into the roles of active sites and electron density redistribution, J. Environ. Chem. Eng. 13 (2025) 115180.
[17] Y. Tong, N. Wang, F. Cheng, X. Huo, Y. Liu, Y. Zhang, X. Cheng, P. Zhou, CuS assisted Fe(III)-induced peracetic acid activation for bisphenol A degradation: significance of synergetic roles of copper and sulfur in enhanced Fenton-like process, Chem. Eng. J. 487 (2024) 150510.
[18] X. Wang, Y. Ding, D.D. Dionysiou, C. Liu, Y. Tong, J. Gao, G. Fang, D. Zhou, Efficient activation of peroxymonosulfate by copper sulfide for diethyl phthalate degradation: performance, radical generation and mechanism, Sci. Total Environ. 749 (2020) 142387.
[19] R. Ma, Z. Chen, W. Xu, R. Yu, Y. Zhang, F. Chen, X. Peng, B.J. Ni, J. Qian, Fe-MOFs/CuS nanocomposite-mediated peroxymonosulfate activation for tetracycline degradation: Boosted dual redox cycles, J. Clean. Prod. 442 (2024) 140885.
[20] A.B. Azzam, A.O. Abd El-Aziz, S.K. Mohamed, Activation of persulfate using CuS synthesized by ultrafast solid-state reaction for removal of organic pollutants from wastewater: economical synthesis, catalytic performance, and mechanism, Sep. Purif. Technol. 284 (2022) 120238.
[21] L. Chen, X. Wang, M. Yuan, B.J. Ni, S. Xia, J. Zhao, Insights into the removal of sulfamethazine and sulfonamide-resistant bacteria from wastewater by Fe-Mn spinel oxide modified cow manure biochar activated peroxymonosulfate: a nonradical pathway regulated by enhanced adsorption and 3d orbital electron reconstruction, Applied Catalysis B: Environment and Energy. 361 (2025) 124652.
[22] R. Ma, G. Zhou, M. Gu, X. Tang, W. Ding, Y. Guan, Y. Jiang, J. Yin, L. Zhang, E. Huixiang Ang, Cobalt leaching inhibition: transforming coordination polymers into spherical Co_3O_4@NC catalysts for accelerated tetracycline degradation via enhanced PMS activation, Appl. Surf. Sci. 648 (2024) 158980.
[23] H. Fu, S. Ma, P. Zhao, S. Xu, S. Zhan, Activation of peroxymonosulfate by graphitized hierarchical porous biochar and $MnFe_2O_4$ magnetic nanoarchitecture for organic pollutants degradation: structure dependence and mechanism, Chem. Eng. J. 360 (2019) 157–170.
[24] G. Cao, Z. Shen, J. Cui, M. Yu, W. Li, Bifunctional activation of peroxymonosulfate over CuS/g-C_3N_4 composite for efficient degradation of tetracycline antibiotics, Chem. Eng. J. 483 (2024) 149082.
[25] M. Liu, H. Zhu, R. Du, W. Zhang, W. Shi, Z. Guo, S. Tang, E.H. Ang, J. Yang, J. Pan, F. Yang, Constructing functional thermal-insulation-layer on Co_3O_4 nanosphere for reinforced local-microenvironment photothermal PMS activation in pollutant degradation, J. Environ. Chem. Eng. 11 (2023) 109939.
[26] Y. Feng, D. Wu, Y. Deng, T. Zhang, K. Shih, Sulfate radical-mediated degradation of sulfadiazine by $CuFeO_2$ rhombohedral crystal-catalyzed peroxymonosulfate: synergistic effects and mechanisms, Environ. Sci. Technol. 50 (2016) 3119–3127.
[27] W. Nie, Q. Mao, Y. Ding, Y. Hu, H. Tang, Highly efficient catalysis of chalcopyrite with surface bonded ferrous species for activation of peroxymonosulfate toward degradation of bisphenol A: a mechanism study, J. Hazard. Mater. 364 (2019) 59–68.
[28] J. Wang, S. Wang, Activation of persulfate (PS) and peroxymonosulfate (PMS) and application for the degradation of emerging contaminants, Chem. Eng. J. 334 (2018) 1502–1517.
[29] H. Jiang, Z. Hu, Y. Ouyang, X. Ji, X. Hu, T. Li, K. Ouyang, P. Wang, H. Wang, X. Hu, Multi-phase CdS loaded on biochar for photocatalytic activation of peroxymonosulfate for thiamethoxam degradation: π-conjugation improves PMS adsorption, Sep. Purif. Technol. 326 (2023) 124842.
[30] D. Zheng, X. Zhao, Y. Wang, X. Dai, K. Guo, C. Xu, N. Zhao, F.J. Xu, Facile construction of polycation/Au@CuS nanohybrids for synergistic gene/photothermal therapy, Chem. Eng. J. 486 (2024) 150271.
[31] J. Pan, B. Gao, P. Duan, K. Guo, X. Xu, Q. Yue, Recycling exhausted magnetic biochar with adsorbed Cu^{2+} as a cost-effective permonosulfate activator for norfloxacin degradation: Cu contribution and mechanism, J. Hazard. Mater. 413 (2021) 125413.
[32] D. Ding, S. Yang, X. Qian, L. Chen, T. Cai, Nitrogen-doping positively whilst sulfur-doping negatively affect the catalytic activity of biochar for the degradation of organic contaminant, Appl. Catal. Environ. 263 (2020) 118348.
[33] S.F. Jiang, L.L. Ling, W.J. Chen, W.J. Liu, D.C. Li, H. Jiang, High efficient removal of bisphenol A in a peroxymonosulfate/iron functionalized biochar system: Mechanistic elucidation and quantification of the contributors, Chem. Eng. J. 359 (2019) 572–583.
[34] Y. Ma, C. Zhang, E.H. Dawolo, N. Ding, H. Liu, Fe/Mn-doped Chlorella biochar for enhanced metronidazole degradation via PMS activation: mechanistic insights into catalytic performance, J. Mater. Chem. C (2025), https://doi.org/10.1039/d5tc01144b.
[35] J. Zhou, X. Yang, Q. Wei, Y. Lan, J. Guo, Co_3O_4 anchored on biochar derived from chitosan (Co_3O_4@BCC) as a catalyst to efficiently activate peroxymonosulfate (PMS) for degradation of phenacetin, J. Environ. Manage. 327 (2023) 116895.
[36] Z. Wang, X.F. Zhang, L. Shu, J. Yao, Copper sulfide integrated functional cellulose hydrogel for efficient solar water purification, Carbohydr. Polym. 319 (2023) 121161.
[37] X. Yang, X. Zhang, Z. Wang, S. Li, J. Zhao, G. Liang, X. Xie, Mechanistic insights into removal of norfloxacin from water using different natural iron ore-biochar composites: more rich free radicals derived from natural pyrite-biochar composites than hematite-biochar composites, Appl. Catal. Environ. 255 (2019) 117752.

[38] C. Wang, J. Tian, Y. Cui, N. Li, X. Cui, B. Yan, G. Chen, Synergy of CoN_3 and CuN_3O_2 sites in single atom-decorated biochar for peroxymonosulfate activation: accelerating the production of $SO4^{\bullet-}$ and •OH, Chem. Eng. J. 496 (2024) 154133.
[39] Z. Xu, Z. Lin, Y. Zeng, H. Yang, Y. Wang, M. Niu, Z. Xiao, J. Luo, Z. Lin, P. Chen, W. Lv, G. Liu, Preparation of Fe-doped coffee ground biochar and activation of PMS for chloroquine phosphate removal, Appl. Surf. Sci. 679 (2025) 161160.
[40] S. Wang, J. Wang, Peroxymonosulfate activation by Co_9S_8@ S and N co-doped biochar for sulfamethoxazole degradation, Chem. Eng. J. 385 (2020) 123933.
[41] Y. Li, Y. Zhou, R. Ni, J. Shang, X. Cheng, Degradation of sulfamethazine sodium salt by peroxymonosulfate activated by biochar supported $CoFe_2S_4$: performance, mechanism and response surface method optimization, J. Environ. Chem. Eng. 10 (2022) 108059.
[42] X. Xie, Z. Guo, H. He, Y. Liu, J. Wei, X. Zhang, W. Wang, X. Wen, Y. Song, Mechanism insights into nitrogen vacancy (-C≡N) effect in Fe-CN for enhancing catalytic ozonation towards ibuprofen degradation: electron donator and hydroxyl groups initiator, Chem. Eng. J. 517 (2025) 164380.
[43] J. Zhang, J. Wei, Z. Guo, Q. Luo, J. Dou, Y. Song, Monodispersed ZIF-67 in situ nucleated on CoAl-LDH nanosheets for efficient carbamazepine degradation via activation of peroxymonosulfate, J. Clean. Prod. 448 (2024) 141546.
[44] X. Liu, L. Wang, T. Fu, G. Xu, J. Han, L. Jiang, F. Qian, G. Zhu, J. Yuan, Y. Song, H. Zhao, J. Dou, Carbon nanotube supported iron phthalocyanine providing efficient electron transfer pathway for water decontamination, Applied Catalysis B: Environment and Energy. 372 (2025) 125303.
[45] D. Luo, H. Zhang, X. An, J. Zhao, C. Feng, J. Yin, M. Luo, T. Wei, Y. Liu, Y. Shi, J. Zhang, B. Lai, Synergistic effects of sulfur-doped carbon dots/permanganate process for DCF degradation: mechanism and pathways, J. Hazard. Mater. 494 (2025) 138567.
[46] Y. Sun, M. Li, M.H. Hadizadeh, F. Xu, OH/O_3-initiated transformation of primidone in AOPs based on the theoretical calculations: mechanisms, kinetics, and eco-toxicity assessments, J. Environ. Chem. Eng. 11 (2023) 109167.
[47] X. Duan, H. Jia, T. Cao, H. Yu, Y. Zhang, Y. Lu, D. Zhou, Nitrate promoted ATZ degradation in Z-scheme $Cs_3Bi_2I_9$/$BiVO_4$ photocatalytic system: coupling •OH and RNS mediated reduction and oxidation, Appl. Catal. B Environ. Energy 352 (2024) 124016.
[48] P. Xu, R. Wei, P. Wang, X. Li, C. Yang, T. Shen, T. Zheng, G. Zhang, $CuFe_2O_4$/diatomite actuates peroxymonosulfate activation process: Mechanism for active species transformation and pesticide degradation, Water Res. 235 (2023) 119843.
[49] W.D. Oh, Z. Dong, G. Ronn, T.T. Lim, Surface-active bismuth ferrite as superior peroxymonosulfate activator for aqueous sulfamethoxazole removal: performance, mechanism and quantification of sulfate radical, J. Hazard. Mater. 325 (2017) 71–81.
[50] H. Lu, M. Sui, B. Yuan, J. Wang, Y. Lv, Efficient degradation of nitrobenzene by Cu-Co-Fe-LDH catalyzed peroxymonosulfate to produce hydroxyl radicals, Chem. Eng. J. 357 (2019) 140–149.
[51] S. Wang, T. Li, X. Cheng, R. Zhu, Y. Xu, Regulating the concentration of dissolved oxygen to achieve the directional transformation of reactive oxygen species: a controllable oxidation process for ciprofloxacin degradation by calcined CuCoFe-LDH, Water Res. 233 (2023) 119744.
[52] J. Guo, H. Zhao, Z. Yang, L. Wang, A. Wang, J. Zhang, L. Ding, L. Wang, H. Liu, X. Yu, Bimetallic sulfides with vacancy modulation exhibit enhanced electrochemical performance, Adv. Funct. Mater. 34 (2024) 2315714.
[53] G. Xu, X. Song, M. Jiang, R. Wang, S. Lian, X. Yang, Synergistic promotion of reaction kinetics for LiPSs at high loadings by interfacial built-in electric field and sulfur vacancies of ternary heterostructure for high-performance Li-S batteries, Applied Catalysis B: Environment and Energy. 362 (2025) 124707.
[54] S. Lu, Z. Liu, J. Wu, J. Xu, Sulfur vacancies form charge transport channels on the S-type heterojunction engineered interface to enhance photocatalytic performance, Surf Interfaces 53 (2024) 104947.
[55] Z. Zhang, J. Wang, H. Zhang, Y. Deng, B. Tan, J. Wang, T. Yang, W. Wang, Construction of S-doped cellulose nanocrystals with edge sulfur vacancies to enhance the generation of $^1O_2$ and promote peroxymonosulfate (PMS) activation, Appl. Surf. Sci. 671 (2024) 160717.
[56] J. Wang, J. Yao, Y. Li, Z. Wei, C. Gao, L. Jiang, X. Wu, S vacancies-introduced chalcopyrite switch radical to non-radical pathways via peroxymonosulfate activation: vital roles of S vacancies, J. Hazard. Mater. 467 (2024) 133751.
[57] K. Rong, X. Li, Q. Yang, Z. Liu, Q. Yao, Z. Zhang, R. Li, L. Zhao, H. Zheng, Removal of aqueous Cr(VI) by green synthesized sulfide iron nanoparticles loaded corn straw biochar: performance, mechanism, and DFT calculations, Appl. Surf. Sci. 670 (2024) 160729.
[58] Y. Yang, Z. Bian, L. Zhang, H. Wang, Bi@$BiO_x(OH)_y$ modified oxidized g-C_3N_4 photocatalytic removal of tetracycline hydrochloride with highly effective oxygen activation, J. Hazard. Mater. 427 (2022) 127866.
[59] D. Wang, Y. He, Y. Chen, F. Yang, Z. He, T. Zeng, X. Lu, L. Wang, S. Song, J. Ma, Electron transfer enhancing the Mn(II)/Mn(III) cycle in MnO/CN towards catalytic ozonation of atrazine via a synergistic effect between MnO and CN, Water Res. 230 (2023) 119574.
[60] S. Yue, L. Chen, M. Zhang, Z. Liu, T. Chen, M. Xie, Z. Cao, W. Han, Electrostatic field enhanced photocatalytic CO_2 conversion on $BiVO_4$ nanowires, Nano-Micro Letters. 14 (2021) 15.
[61] H. Sun, L. Li, Y. Chen, H. Kim, X. Xu, D. Guan, Z. Hu, L. Zhang, Z. Shao, W. Jung, Boosting ethanol oxidation by NiOOH-CuO nano-heterostructure for energy-saving hydrogen production and biomass upgrading, Appl. Catal. Environ. 325 (2023) 122388.
[62] C. Zhao, L. Meng, H. Chu, J.F. Wang, T. Wang, Y. Ma, C.C. Wang, Ultrafast degradation of emerging organic pollutants via activation of peroxymonosulfate over Fe_3C/Fe@N-C-x: singlet oxygen evolution and electron-transfer mechanisms, Appl. Catal. Environ. 321 (2023) 122034.
[63] Q. Zhou, C. Song, P. Wang, Z. Zhao, Y. Li, S. Zhan, Generating dual-active species by triple-atom sites through peroxymonosulfate activation for treating micropollutants in complex water, Proc. Natl. Acad. Sci. 120 (2023) e2300085120.
[64] F. Wang, Z. Bian, W. Zhang, L. Zheng, Y. Zhang, H. Wang, Fluorine-free MXene activate peroxymonosulfate to remove tetracyclic antibiotics, Sep. Purif. Technol. 314 (2023) 123549.
[65] X. Zhu, L. Ge, W. Yan, S. Yang, G. Wang, D. Miao, P. Jin, Peroxymonosulfate activation by immobilized $CoFe_2O_4$ network for the degradation of sulfamethoxazole, J. Environ. Chem. Eng. 10 (2022) 107781.
[66] R. Ma, J. Song, H. Ding, Q. Han, X. Tang, F. Lv, S. Wen, J. Yin, E.H. Ang, Decoding the entropy-stabilized matrix of high-entropy layered double hydroxides: harnessing strain dynamics for peroxymonosulfate activation and tetracycline degradation, J. Colloid Interface Sci. 680 (2025) 676–688.
[67] L. Chang, X. Xue, Q. Deng, X. Xie, X. Zhang, C. Cheng, H. Chai, Y. Huang, Modulating the electronic structure of Co center via MgO@C co-doping for PMS activation to remove levofloxacin, Sep. Purif. Technol. 321 (2023) 124151.
[68] Q. Jiang, Y. Ma, P. Zhao, X. Li, Y. Shao, X. Xu, Electronic structure regulation of Fe sites by coordinating moieties in the Fenton-like process enables tunable water decontamination, Environ. Sci. Technol. 59 (2025) 14182–14192.
[69] P. Yang, Z. Cao, Y. Long, D. Liu, W. Huang, S. Zhan, M. Li, Regulating the local electronic structure of copper single atoms with unsaturated B,O-coordination for selective $^1O_2$ generation, ACS Catal. 13 (2023) 12414–12424.
[70] W. Zhang, S. Zhang, Z. Chen, Z. Zhang, Cobalt-ferrite functionalized graphitic carbon nitride ($CoFe_2O_4$@g-C_3N_4) nanoconfined catalytic membranes for efficient water purification: performance and mechanism, J Mater Chem A 11 (2023) 18933–18944.
[71] Z. Liu, S. Pan, F. Xu, Z. Wang, C. Zhao, X. Xu, B. Gao, Q. Li, Revealing the fundamental role of MoO_2 in promoting efficient and stable activation of persulfate by iron carbon based catalysts: efficient Fe^{2+}/Fe^{3+} cycling to generate reactive species, Water Res. 225 (2022) 119142.
[72] J.Q. Li, Z.W. Zhou, X. Li, Y.L. Yang, J.F. Gao, R. Yu, H.P. Wang, N. Wang, Synergistically boosting sulfamerazine degradation via activation of peroxydisulfate by photocatalysis of Bi_2O_3-TiO_2/PAC under visible light irradiation, Chem. Eng. J. 428 (2022).
[73] Y. Huang, J. Zhang, Z. Guo, H. Zang, M. Zheng, T. Hao, J. Wei, Bimetallic Fe-Mo modified N-doped carbon materials activating peroxymonosulfate for acetaminophen degradation: synergistic effects of free radicals and electron transfer process, Environ. Res. 270 (2025) 121013.
[74] Y. Guo, G. Yu, U. von Gunten, Y. Wang, Evaluation of the role of superoxide radical as chain carrier for the formation of hydroxyl radical during ozonation, Water Res. 242 (2023) 120158.
[75] Y. Zhang, Y. Guo, J. Fang, K. Guo, G. Yu, Y. Wang, Characterization of UV/chlorine process for micropollutant abatement by probe compound-based kinetic models, Water Res. 237 (2023) 119985.
[76] M. Zhu, D. Guan, Z. Hu, H.J. Lin, C.T. Chen, H.S. Sheu, S. Wang, J. Zhou, W. Zhou, Z. Shao, Synergistic effects in ordered Co oxides for boosting catalytic activity in advanced oxidation processes, Appl. Catal. Environ. 297 (2021) 120463.
[77] D. Guan, H. Xu, Y.C. Huang, C. Jing, Y. Tsujimoto, X. Xu, Z. Lin, J. Tang, Z. Wang, X. Sun, L. Zhao, H. Liu, S. Liu, C.T. Chen, C.W. Pao, M. Ni, Z. Hu, Z. Shao, Operando studies redirect spatiotemporal restructuration of model coordinated oxides in electrochemical oxidation, Adv. Mater. 37 (2025) 2413073.
[78] Z. Qing, Q. Qin, Z. Yang, L. Wang, X. Yang, Y. Liu, S. Zhang, H. Zhao, J. Chen, Simple sulfuration of layered double hydroxide modulating efficient $^1O_2$ formation in peroxymonosulfate activation: in-situ regeneration of catalyst, Chem. Eng. J. 517 (2025) 164190.